ANNALS OF GEOPHYSICS, 69, 2026; doi:10.4401/ag-9474
OPEN ACCESS

State-of-the-Art Computerized Ionospheric Tomography over Africa and Türkiye

Sinem Deniz Yenen[*,1,2], Feza Arikan[2], Orhan Arikan[3]

(1) ASELSAN Inc., Ankara, Türkiye
(2) Hacettepe University, Department of Electrical and Electronics Engineering, Ankara, Türkiye
(3) Bilkent University, Department of Electrical and Electronics Engineering, Ankara, Türkiye

Article history: received October 10, 2025; accepted February 12, 2026

Abstract

This study presents an application of the 4-D computerized ionospheric tomography (CIT) algorithm, IONOLAB-Fusion, developed for reconstructing ionospheric electron density as a function of height, latitude, longitude, and time. The algorithm integrates data from ground-based Global Positioning System (GPS) receivers and Radio Occultation (RO) satellite measurements to generate high-fidelity ionospheric models under varying observational conditions. In this study, IONOLAB-Fusion is applied to two distinct regions: Türkiye, representing a well-instrumented midlatitude environment in the Northern Hemisphere, and Africa, encompassing both equatorial and midlatitude sectors characterized by limited receiver coverage. Over Türkiye, validation against Global Ionospheric Maps (GIMs) shows that the algorithm significantly outperforms Total Electron Content (TEC) estimates from the IRI-Plas model, achieving improvements of up to 90% during quiet ionospheric conditions. Over Africa, despite severe data sparsity, improvements of up to 77% on quiet days and 63% on disturbed days relative to GIMs are achieved. Further validation using ionosonde vertical electron density profiles in South Africa shows consistency between observations and reconstructions, with accuracy gains of over 84% and over 53% for quiet and disturbed conditions, respectively. Additionally, a case study conducted using RO data shows that reconstructions without and with RO measurements improve upon IRI-Plas by 50% and 54%, respectively, highlighting the added value of RO observations. These findings confirm that IONOLAB-Fusion provides robust, accurate, computationally efficient, and physically consistent reconstructions across regions with both dense and sparse observation networks, demonstrating strong potential for regional and global ionospheric modeling, space weather monitoring, and improved global navigation system reliability.

Keywords: Ionosphere; computerized ionospheric tomography; IRI-Plas; GPS; LEO

1. Introduction

Computerized Ionospheric Tomography (CIT) has emerged as a powerful remote sensing technique for reconstructing the spatio-temporal electron density distribution by combining the measurements of line-of-sight Total Electron Content (TEC) derived from Global Positioning System (GPS) observations with mathematical inversion algorithms (Arikan et al., 2007; Austen et al., 1988).

Early implementations of CIT were 2-D and employed iterative algebraic reconstruction methods such as the Algebraic Reconstruction Technique (ART) and Multiplicative ART (MART), which required an initial density estimate and were sensitive to data noise and limited spatial coverage (Austen et al., 1988; Jin and Li, 2018; Raymund et al., 1990; Yavuz et al., 2005). Although these methods provided early insights into the ionosphere's vertical structure, their assumptions about horizontal homogeneity and limited convergence rates restricted their applicability in regions with sparse GPS receiver networks. As the number of GPS receivers increased worldwide, 3-D and 4-D CIT algorithms are developed, enabling finer spatial and temporal resolutions (Bust and Mitchell, 2008; Garcia and Crespon, 2008; Lu et al., 2021; Zhai et al., 2020). However, the inherent ill-conditioning of the tomographic inversion problem, caused by uneven data distribution and limited satellite-receiver geometry, continues to pose challenges for stable and accurate reconstructions.

In parallel with these developments, data assimilation techniques have gained widespread use in ionospheric imaging, where heterogeneous measurements are integrated into a background model to achieve a more accurate state estimation for the specific region of interest. Representative examples include the Multi-Instrument Data Analysis System (MIDAS) (Mitchell and Spencer, 2003; Spencer and Mitchell, 2007), as well as various regional ionospheric data assimilation frameworks driven by multiple data sources (Ssessanga et al., 2019). However, due to the lower number of observations available at regional scales, these global assimilation models may underperform in accurately characterizing local ionospheric states in specific regions of interest.

To overcome data sparsity, function-based approaches have been adopted in the literature, including Spherical Cap Harmonics (Al-Franek, 2013), Haar Wavelets (Amerian et al., 2010), B-Spline functions (Zeilhofer et al., 2009), and Slepian functions (Farzaneh and Forootan, 2018). In these models, the electron density is expressed as a weighted sum of orthogonal basis functions. As outlined in (Yenen and Arikan, 2024) these methods reformulate the inversion into a coefficient estimation problem, improving stability by constraining the solution space. Yet, representing fine-scale ionospheric structures often requires a large number of coefficients, raising computational costs and memory requirements and such models rarely provide explicit descriptions of how ray paths and path lengths are incorporated in the forward model. Consequently, although these techniques yield to solutions, they often fail to capture the anisotropic and layered behavior of the ionosphere, especially under disturbed geomagnetic conditions (Yenen and Arikan, 2024).

The IONOLAB research group has contributed significantly to addressing these challenges by developing a family of ionospheric reconstruction and modeling tools. The IONOLAB-STEC algorithm provides accurate estimation of Slant Total Electron Content (STEC) from dual-frequency GPS observations, serving as the foundation for measurement-based ionospheric characterization (Arikan et al., 2003; Arikan et al., 2004; Arikan et al., 2008; Koroglu and Arikan, 2020; Nayir et al., 2007; Sezen et al., 2013). Complementing this, using the International Reference Ionosphere extended to the Plasmasphere (IRI-Plas), the IRI-Plas-STEC model computes synthetic STEC values between satellite-receiver pairs, thereby enabling the generation of realistic forward-modeled TEC data for validation and hybrid tomography (Arikan et al., 2016; Tuna et al., 2014). The IONOLAB-Ray algorithm further enhances this framework by tracing radio-wave propagation through a refractive ionospheric medium according to the Appleton-Hartree equation, incorporating both geomagnetic and plasma frequency effects (Erdem et al., 2015; Erdem and Arikan, 2017; Erdem, 2017; Erdem and Arikan, 2018). Building upon these foundations, the IONOLAB-CIT algorithm introduced an iterative optimization scheme that adjusts model parameters such as the F2-layer critical frequency (foF2) and its corresponding peak height (hmF2) to minimize discrepancies between synthetic and observed TEC values (Tuna et al., 2015). IONOLAB-CIT has demonstrated strong performance in midlatitude regions, particularly over Türkiye, by integrating GPS-derived TEC data with model-based constraints to reconstruct regional 4-D electron density fields (Tuna et al., 2018). However, its performance degrades in equatorial and polar regions, where nonlinear gradients and multi-peak vertical profiles dominate.

To address these limitations and achieve a more general, closed-form, and computationally efficient tomographic solution, this study provides an application of the IONOLAB-Fusion algorithm, a novel Singular Value Decomposition (SVD)-based 4-D Computerized Ionospheric Tomography (CIT) framework. The IONOLAB-Fusion algorithm provides a 4-D CIT framework for reconstructing electron density as a function of height, latitude, longitude, and time (Yenen and Arikan, 2024). Building upon the methodology proposed in (Erturk et al., 2009), the approach has been advanced into a SVD-based closed–form reconstruction algorithm, offering a stable, non-iterative solution to the ionospheric inverse problem. The model matrix generation process is optimized by incorporating solar activity levels together with hourly and monthly variations in latitude, longitude, height, and local time, enabling realistic reconstructions for any selected region. For each voxel, the background electron density

values are derived from the IRI-Plas model through the IONOLAB-RAY framework, ensuring that the refractive index accurately reflects the anisotropic and temporally variable ionosphere. The sampling matrix is expanded to include STEC paths between ground-based GPS receivers and GPS satellites, as well as between receivers on-board LEO satellites and GPS satellites. To achieve uniform spatial sampling, augmented virtual receivers are introduced in under-observed regions such as oceans and deserts, while redundant paths in densely instrumented areas are adaptively decimated. The LEO satellite geometry is computed within a temporal wide-sense stationarity window and further augmented to maximize spatial coverage. The algorithm can utilize both measured STEC obtained from IONOLAB-STEC and synthetic STEC computed from the ionospheric model with IRI-Plas-STEC when observations are sparse. After constructing the model and sampling matrices, SVD is applied to isolate significant physical bases that capture the dominant electron density variations, and the reconstruction coefficients are estimated in closed form using a least-squares approach. Owing to this design, the algorithm typically requires only one or two dominant bases for accurate 4-D reconstruction, resulting in a fast, robust, and user-configurable tomography system.

In (Yenen and Arikan, 2024), IONOLAB-Fusion has been successfully applied to the European region, a midlatitude area in the Northern Hemisphere, to evaluate the accuracy, robustness, and reliability of the algorithm. Europe provides an ideal testbed for this purpose, as it features a dense network of ground-based GPS receivers and a significant number of ionosondes (Feltens, 2003).

In this study, the state-of-the-art 4-D computerized ionospheric tomography algorithm, IONOLAB-Fusion, is applied to Türkiye, a midlatitude region in the Northern Hemisphere, and to the African ionosphere, which covers both Kenya and midlatitude regions in the Southern Hemisphere. Türkiye and South Africa provide important case regions for evaluating the performance of IONOLAB-Fusion, as they are located at geographically and geomagnetically conjugate latitudes in the Northern and Southern Hemispheres, respectively. This conjugate configuration allows for comparative assessments of ionospheric behavior under similar geomagnetic conditions. The inclusion of these two regions enables a balanced examination of the algorithm's accuracy across distinct midlatitude environments. Furthermore, Kenya introduces a new equatorial test region, extending the application of IONOLAB-Fusion beyond midlatitude studies. The equatorial ionosphere, characterized by the presence of the Equatorial Ionization Anomaly (EIA), presents a more challenging environment for computerized ionospheric tomography. Applying IONOLAB-Fusion to Kenya therefore provides the first demonstration of closed-form 4-D ionospheric electron density reconstruction in the equatorial region using augmented observations, highlighting the algorithm's robustness and adaptability under highly dynamic ionospheric conditions.

In addition to regional validation, this study presents a multi-method comparative evaluation of IONOLAB-Fusion against established ionospheric reconstruction techniques. For the South Africa region, electron density reconstructions obtained using IONOLAB-Fusion are benchmarked against alternative function-based reconstruction approaches. This comparative analysis provides an objective performance assessment and demonstrates the robustness and reconstruction capability of IONOLAB-Fusion.

Moreover, this study introduces, for the first time, the graphical user interface (GUI) of IONOLAB-Fusion, developed to enhance accessibility, reproducibility, and operational usability by providing a structured interface to the algorithm's high-dimensional configuration space. The GUI provides an intuitive and interactive workflow, enabling users to easily configure processing parameters, select geographic and temporal domains, visualize intermediate products, and generate high-fidelity reconstructions without requiring extensive technical expertise. All preprocessing steps, including receiver network optimization, model matrix construction, reconstruction, and data storage are performed automatically based on user-defined inputs. The presented results collectively demonstrate the algorithm's versatility, accuracy, and user-oriented design, underscoring its potential as a robust and scientifically rigorous tool for ionospheric modeling across regions with both dense and sparse observational infrastructures.

A concise description of the IONOLAB-Fusion methodology is presented in Section 2, followed by the results and discussion in Section 3. The conclusion is provided in Section 4.

2. A Brief Summary of IONOLAB-Fusion

IONOLAB-Fusion is a 4-D model-based tomography framework capable of reconstructing electron density across height, latitude, longitude, and time using both ground-based GPS receivers and LEO radio occultation (RO) observations. The algorithm integrates physically guided modeling with matrix decomposition, providing closed-form, noise resilient reconstructions applicable to both regional and global scales.

The GUI serves as the primary operational layer through which all algorithmic configurations, including spatial discretization, vertical domain definition, receiver selection and augmentation, ray geometry, and model matrix generation, are defined in a transparent and reproducible manner. The reconstruction date and time are specified directly through the GUI together with the region boundaries and corresponding latitude and longitude resolutions. The vertical reconstruction domain is also user-defined, allowing the height to be specified using either regular or irregular resolution intervals. For regular intervals, the height range extends from a user-defined minimum height to a user-defined maximum height with a uniform height resolution. For irregular intervals, different height resolutions may be assigned to selected altitude ranges as needed. Alternatively, height values can be defined as an array and entered through the GUI, providing full flexibility in configuring the vertical reconstruction grid (Fig. 1). Based on this information, the algorithm automatically identifies all GPS receivers located within the selected region.

The GUI evaluates the density and uniformity of available receiver stations through a uniform square sampling procedure. This procedure is designed to construct the tomographic measurement set using an optimal number of receivers within the region of interest, ensuring spatial uniformity as much as possible while avoiding multiple ray paths passing through the same or closely spaced voxels in both horizontal and vertical directions (Sayin et al., 2008). When redundant receivers are detected within a single sampling cell, they are removed to prevent oversampling. Conversely, if certain grid cells lack coverage, virtual or augmented ground-based receivers can be added in those locations, at the user's discretion, to maintain geometric balance and ensure sufficient data distribution for inversion.

Users can then choose between two strategies for generating the model matrix, either the hourly-monthly formation using days with similar solar activity levels or the retrospective formation using the most recent days

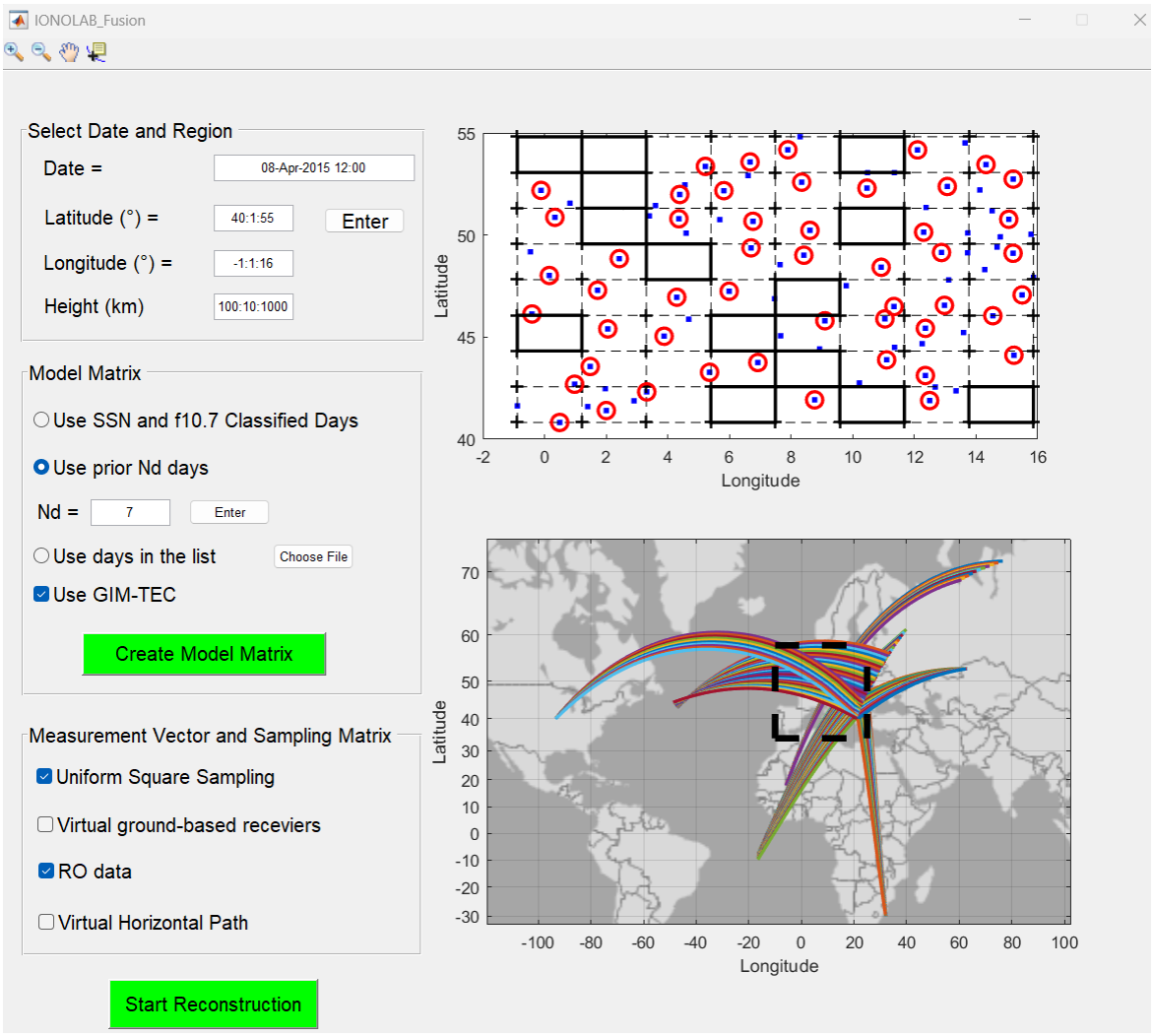

Figure 1. IONOLAB-Fusion GUI showing (top) the uniform square sampling and receiver distribution within the selected region, and (bottom) the corresponding GPS and LEO ray-path geometry used for tomography.

before the reconstruction. An additional option allows inclusion of GIM-TEC data during model matrix generation to improve correspondence with actual ionospheric conditions.

Once the desired parameters are defined, activating the "Create Model Matrix" command initiates the generation of the background electron density structure. If a model matrix corresponding to the selected region, date, and time already exists in the database, the algorithm reuses the existing matrix rather than generating a new one, thereby improving computational efficiency.

When the "Start Tomography" command is executed, the sampling matrix and measurement vector are computed using the selected ray paths. During this process, IONOLAB-Fusion automatically retrieves the relevant GPS and LEO satellite ephemeris data for the specified time interval and determines all feasible signal paths between transmitters and receivers. The user may optionally enable additional ray types – such as links between GPS satellites and LEO receivers, as well as virtual vertical and slant paths – to enhance spatial sampling. These ray geometries are dynamically visualized within the GUI on either a global or regional map, as shown in Fig. 1, providing immediate feedback on the sampling distribution prior to reconstruction. The tomographic reconstruction is then completed through the combined use of the model matrix, sampling matrix, and measurement vector, yielding the final 4-D electron density distribution. The resulting reconstruction outputs are automatically saved as a MATLAB (.mat) file, enabling users to conduct further analysis, visualization, or validation within external processing environments.

The construction of the model matrix is discussed in detail in the following subsection.

2.1 Model Matrix Construction

The central component of IONOLAB-Fusion is the model matrix, which represents the background ionosphere within the reconstruction domain. The ionosphere is first divided into 3-D spherical voxels using the IONOLAB-mRAY algorithm, developed from IONOLAB-RAY algorithm (Yenen, 2024), as given in Fig. 2, according to user-defined spatial and temporal resolutions. Each voxel is uniquely indexed in lexicographical order with respect to height, latitude, longitude, and time, enabling the 4-D ionosphere to be represented as a 1-D vector and efficiently mapped into a 2-D matrix form. This structure ensures computational efficiency and ease of handling during inversion.

To construct the model matrix, the background electron density of each voxel is computed using the IRI-Plas ionospheric model. Electron density profiles from multiple representative days are combined to form columns of the matrix, collectively capturing ionospheric behavior under varying solar and geomagnetic conditions. The number of days included can be freely selected by the user depending on the intended application. Two main strategies are available.

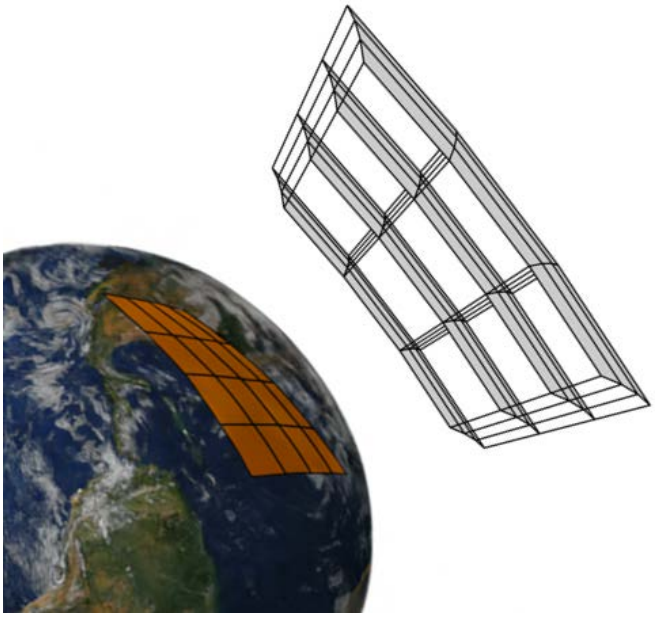

Figure 2. Illustration of a 3-D spherical voxel model.

In hourly-monthly model matrix formation, electron densities are computed for specific hours across several days within months that share similar solar activity levels (Ardic, 2023). By including both quiet and disturbed days, the resulting model matrix captures diurnal and seasonal variability, ensuring that the SVD later extracts physically meaningful basis vectors representing diverse ionospheric states. Alternatively in retrospective model matrix formation, the model matrix can be formed using electron density values from a selected number of preceding days (typically one to three) before the tomography date. This approach supports near-real-time reconstructions and maintains temporal continuity, making it suitable for operational monitoring and forecasting.

Each entry in the model matrix corresponds to the electron density of a specific voxel at a given epoch. The inclusion of a wider range of ionospheric conditions enhances the representativeness of the model and reduces the number of significant singular values required for accurate reconstruction. The GUI of IONOLAB-Fusion automatically generates the model matrix once the user specifies only the region of interest, spatial resolution, date and time of tomography, and temporal resolution.

2.2 Singular Value Decomposition and Basis Selection

After the model matrix is formed, Singular Value Decomposition (SVD) is applied to extract its principal components. SVD separates the model matrix into orthogonal left and right singular bases and a diagonal matrix containing singular values arranged in descending order. These singular values represent the contribution (or energy) of each corresponding basis vector. By examining their cumulative energy, IONOLAB-Fusion automatically identifies the subset of dominant singular values that define the signal subspace, while the remaining components are discarded as noise. In most midlatitude and equatorial cases, only one or two dominant basis vectors are sufficient to capture the ionospheric structure, enabling a compact and efficient reconstruction.

2.3 Measurement Vector and Sampling Matrix

IONOLAB-Fusion requires minimal user input to complete a tomography process. When the operator defines the region boundaries, spatial and temporal resolutions, and the date and time of the reconstruction, the tomography process can be executed. Receiver coordinates can be retrieved automatically from the International GNSS Service (IGS), which maintains a global network of more than 500 stations, or predefined coordinates can be imported by the user. The algorithm then automatically detects all ground-based receiver stations within the selected region. The adequacy and spatial uniformity of the station distribution are evaluated to perform uniform square sampling. If the region lacks sufficient receiver coverage, augmented receivers are automatically introduced in sparse areas to ensure homogeneous sampling. In regions with dense receiver clusters, redundant stations are reduced to maintain even spatial representation.

GPS ephemeris data is automatically downloaded for the specified reconstruction time. For each ground-based and augmented receiver, GPS satellites with an elevation angle greater than 40° are identified, and receiver-satellite pairs are formed accordingly. Users are prompted to indicate whether they wish to include LEO satellites in the tomography, if selected, corresponding ephemeris data are automatically obtained, and LEO-GPS pairs are established based on line-of-sight visibility. The user is also given the option to include virtual LEO rays, which further improve spatial coverage by augmenting the geometry of observation paths.

The Slant TEC (STEC) between each receiver-satellite pair is computed using the IONOLAB-STEC algorithm for real GPS observations and IRI-Plas-STEC for augmented or virtual paths and the measurement vector is constructed using these STEC values.

Ray propagation through the ionosphere is modeled using IONOLAB-mRAY, which traces each signal path voxel by voxel. The wave is assumed to propagate under free-space conditions until it reaches the ionosphere, where it is refracted according to Snell's law (Erdem et al., 2015; Erdem and Arikan, 2017; Erdem, 2017; Erdem and Arikan, 2018; Yenen and Arikan, 2024). For every ray formed between receiver-GPS pairs, the intersection points between the ray and each spherical voxel are recorded, and the refractive index is computed using the Appleton-Hartree equation based on parameters from the IGRF-13 geomagnetic model and background electron densities from IRI-Plas. The total path length traveled within each voxel is stored in the sampling matrix, which serves as the geometric mapping between the observation data and the electron density distribution.

2.4 Closed-Form Reconstruction

The basis matrix, composed of the significant singular vectors extracted from the model matrix, represents the key spatial and temporal patterns of the ionosphere. The coefficient vector defines how strongly each basis pattern contributes to the reconstruction. The algorithm combines the measured TEC values with the corresponding sampling information and basis functions to estimate these coefficients in a least-squares sense. This yields a closed-form reconstruction of the ionospheric electron density, avoiding the convergence and stability issues common in iterative methods. The final output is a 4-D distribution of electron density that evolves consistently with both spatial geometry and temporal dynamics.

The complete algorithmic description and associated flowcharts corresponding to Sections 2.1-2.4 can be found in Yenen and Arikan (2024). In summary IONOLAB-Fusion offers a unified, automated, and physically consistent approach to ionospheric tomography. Its integration of real, augmented, and virtual observations enables reconstruction even in sparse regions. The GUI simplifies complex modeling tasks into an intuitive and reproducible workflow, allowing users to visualize receiver networks, ray geometries, and model matrix configurations before reconstruction. By combining automatic data acquisition, SVD-based compression, and flexible user control, IONOLAB-Fusion provides a robust, high-resolution, and region-independent framework for ionospheric electron density estimation. In the following section, this approach is applied to the regions in Africa and Türkiye to assess its reconstruction capability under varying ionospheric conditions.

3. Results

In this section the results obtained from the application of the IONOLAB-Fusion algorithm to Kenya, South Africa and Türkiye are presented. The selected regions provide a comprehensive framework for evaluating the performance and adaptability of the IONOLAB-Fusion algorithm under distinct ionospheric and observational conditions. Kenya, situated near the magnetic equator, represents a new equatorial test region that extends the application of IONOLAB-Fusion beyond midlatitude domains. The region poses a major challenge for computerized ionospheric tomography due to the absence of ground-based GPS receiver stations and the highly dynamic nature of the Equatorial Ionization Anomaly (EIA). South Africa, located at midlatitudes in the Southern Hemisphere, serves as a geomagnetically conjugate counterpart to Türkiye. While the region hosts only a limited number of GPS receivers, it provides valuable insight into how the algorithm performs under limited data availability. Comparative analysis between South Africa and Türkiye allows for the examination of hemispheric asymmetries and the algorithm's consistency under similar geomagnetic conditions. In contrast, Türkiye, located at Northern Hemisphere midlatitudes, benefits from a dense network of continuously operating GPS receiver stations. This extensive coverage allows for high resolution reconstructions, offering an optimal setting to assess the accuracy, reliability, and internal consistency of IONOLAB-Fusion.

The region of interest, encompassing Kenya, spans latitudes between 5°N and 5°S and longitudes between 33°E and 43°E. The boundary of the expanded region is situated between 13°N and 10°S latitude and 25°E and 47°E longitude, as shown in Fig. 3a. The ground-based receivers are optimized with 20% sampling rate using uniform square sampling with the inclusion of augmented virtual receivers, as illustrated in Fig. 3b.

The ionosphere is divided into 3-D voxels with resolutions optimized in accordance with the limitations of IRI-Plas, selecting $\theta = 1°$ for latitude and $\phi = 1°$ for longitude. In the IONOLAB-Fusion algorithm, the height resolution can be configured either uniformly at regular intervals or non-uniformly based on the significance of the electron density distribution. In this study, the heights set for Kenya and South Africa regions follows, 10 km between 90 km and 600 km, 100 km between 600 km and 1,300 km, and 500 km between 1,300 km and 2,800 km. The upper boundary of 2,800 km was selected to adequately capture the full background ionospheric contribution. Above this altitude, variations in Total Electron Content (TEC) have a minimal impact on the reconstruction results.

For Kenya and South Africa regions region, the algorithm is demonstrated by forming the model matrix using the hourly-monthly median structure of the ionospheric background model, with 90 days from Moderately Solar Active years, specifically April of 2003, 2004 and 2012. The algorithm is tested on both quiet and disturbed days from MSA years.

Geomagnetic activity levels are characterized using the Kp, Dst, and AE indices following standard conventions in the literature (Sezen et al., 2018; Gulyaeva et al., 2018; Yenen et al., 2016). The Kp index provides a global measure

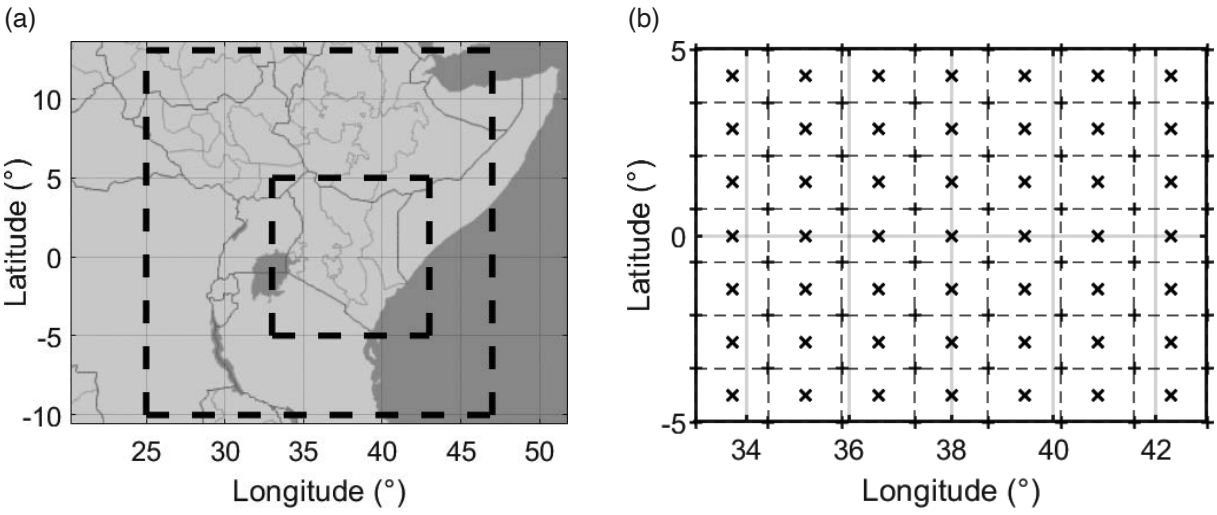

Figure 3. (a) Region of interest within the enlarged region, (b) The virtual ground-based receiver stations indicated with (×).

of geomagnetic activity over three-hour intervals, where values greater than 3 indicate disturbed conditions. The Dst index quantifies the intensity of magnetic storms based on low-latitude geomagnetic field variations, with values lower than −30 nT corresponding to storm-time conditions. The AE index represents auroral zone geomagnetic activity, and values exceeding 500 nT are considered indicative of disturbed conditions. Based on these established thresholds, 17 April 2011 ($Kp_{max} = 1.7$, $Dst_{min} = -3$ nT, $AE_{max} = 206$ nT) and 8 April 2015 ($Kp_{max} = 1.7$, $Dst_{min} = -8$ nT, $AE_{max} = 175$ nT) were classified as geomagnetically quiet days. In contrast, 24 April 2012 ($Kp_{max} = 6.7$, $Dst_{min} = -120$ nT, $AE_{max} = 952$ nT) and 25 April 2013 ($Kp_{max} = 3$, $Dst_{min} = -36$ nT, $AE_{max} = 461$ nT) were classified as disturbed days due to elevated storm indices consistent with geomagnetic storm conditions. The days presented are selected to represent diverse ionospheric conditions rather than to maximize reported accuracy. These cases demonstrate algorithm capabilities across operational conditions.

In Fig. 4, we present slice representations of electron density reconstructions obtained from IONOLAB-Fusion within a selected region of the ionosphere for both quiet and disturbed days at different times, displayed in the leftmost column. The middle column shows electron densities calculated using the IRI-Plas model for the same dates and times. The rightmost column depicts the differences between the electron density reconstructions and the densities calculated from the IRI-Plas model. The reconstruction results utilized only the ground-based receivers in the IONOLAB-Fusion algorithm. In Figs. 4a, 4d, 4g and 4j electron density is reconstructed for 25 April 2013 ionospheric disturbed day, at 03:00 UT, 8 April 2015 ionospheric quiet day, at 12:00 UT, 17 April 2011 ionospheric quiet day, at 18:00 UT and 24 April 2012 ionospheric disturbed day, at 23:00 UT, respectively. The slice heights are selected between 100 km and 500 km with a resolution of 100 km.

Figure 4a illustrates the reconstructed electron density distribution for 25 April 2013 at 03:00 UT. During nighttime hours, ionization levels are relatively low, with the maximum electron density observed around 300 km altitude over the northwestern and eastern parts of the region. Figure 4d shows the electron density for 17 April 2011 at 12:00 UT, when solar illumination is at its peak. Consequently, the ionosphere exhibits its highest electron density, reaching up to 400 km altitude. In Fig. 4g, the electron density decreases as the Sun sets toward the west, with the peak now shifting to the southwestern portion of the region. Finally, Fig. 4j presents the distribution for 24 April 2012 at 23:00 UT. Since ionization primarily depends on solar radiation, a general reduction in electron density is observed at all altitudes after sunset. The comparison between electron densities reconstructed by IONOLAB-Fusion and those derived from the IRI-Plas model throughout the day indicates an agreement, with differences not exceeding a value of 7×10^{11} in electron density units.

Total Electron Content (TEC) values for all latitude and longitude points within a given region are determined by multiplying the electron density within each voxel by the corresponding voxel height increment and summing these contributions across the entire height range. The Global Ionospheric Maps (GIM) provided by the International GNSS Service (IGS) are widely recognized as reliable ionospheric data products. In this study, the GIM obtained from the Center for Orbit Determination in Europe (CODE) is utilized to evaluate the quality of TEC estimates derived from IONOLAB-Fusion. Additionally, TEC values computed using the IRI-Plas model are compared with GIM, serving as

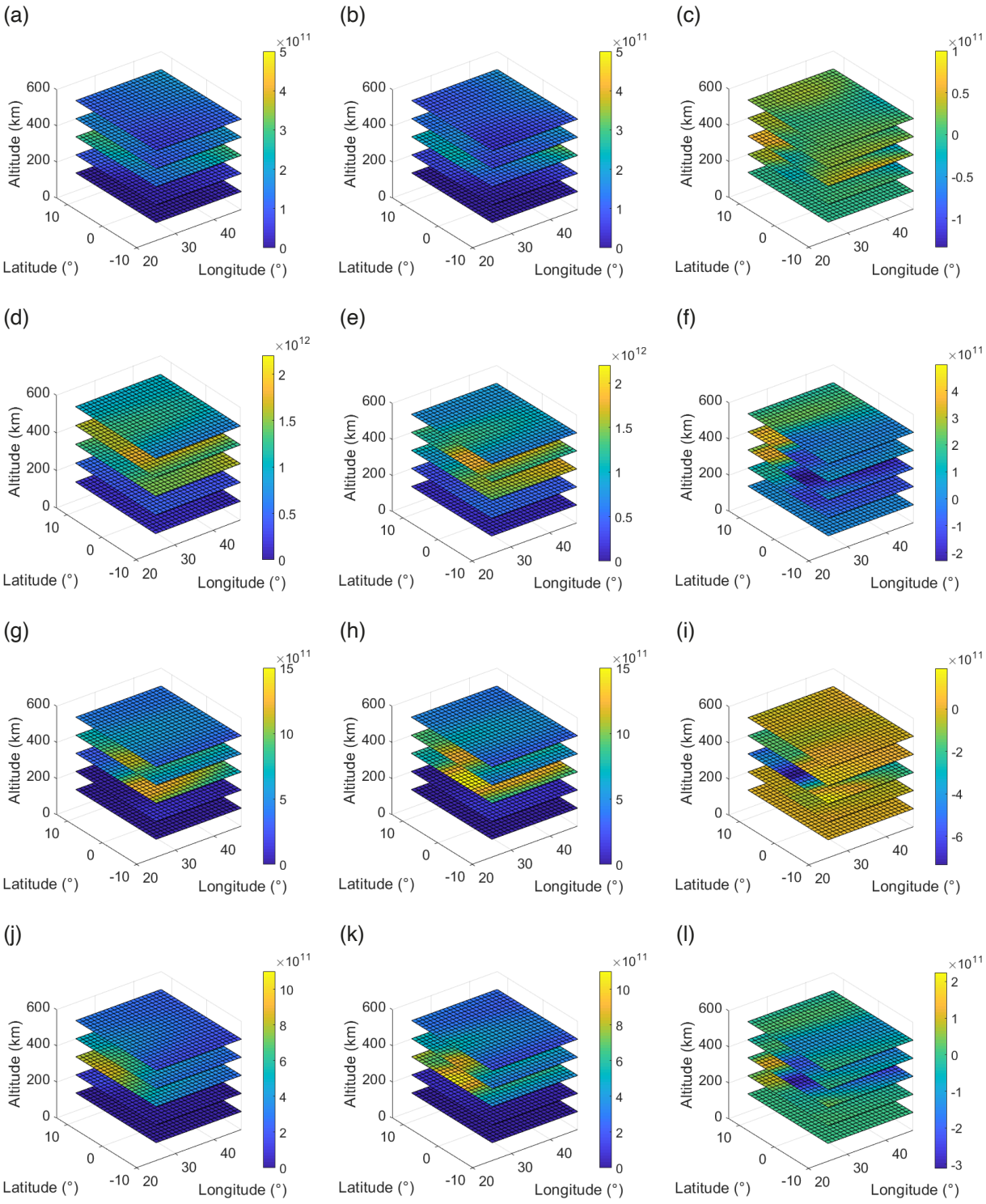

Figure 4. Slices of electron densities with 100 km resolution for different dates and times: (a) reconstructed using IONOLAB-Fusion on 25 April 2013, at 03:00 UT (disturbed day), (b) calculated by IRI-Plas on 25 April 2013, at 03:00 UT, (c) the difference between IONOLAB-Fusion and IRI-Plas for 25 April 2013, at 03:00 UT, (d) reconstructed using IONOLAB-Fusion on 8 April 2015, at 12:00 UT (quiet day), (e) calculated by IRI-Plas on 8 April 2015, at 12:00 UT, (f) the difference between IONOLAB-Fusion and IRI-Plas for 8 April 2015, at 12:00 UT, (g) reconstructed using IONOLAB-Fusion on 17 April 2011, at 18:00 UT (quiet day), (h) calculated by IRI-Plas on 17 April 2011, at 18:00 UT, (i) the difference between IONOLAB-Fusion and IRI-Plas for 17 April 2011, at 18:00 UT, (j) reconstructed using IONOLAB-Fusion on 24 April 2012, at 23:00 UT (disturbed day), (k) calculated by IRI-Plas on 24 April 2012, at 23:00 UT, (l) the difference between IONOLAB-Fusion and IRI-Plas for 24 April 2012, at 23:00 UT.

a reference for validation. TEC computations from IONOLAB-Fusion electron density profiles are performed using the IRI-Plas-STEC algorithm (Sezen et al., 2013) for each latitude and longitude grid point across the reconstruction height range. The resolution of CODE-GIM, originally 2.5° in latitude and 5° in longitude, interpolated to a finer resolution of 1° in both latitude and longitude to match the reconstruction grid. Figure 5 shows representative TEC maps for 25 April 2013 (disturbed day) at 03:00 UT, 8 April 2015 (quiet day) at 12:00 UT, 17 April 2011 (quiet day) at 18:00 UT,

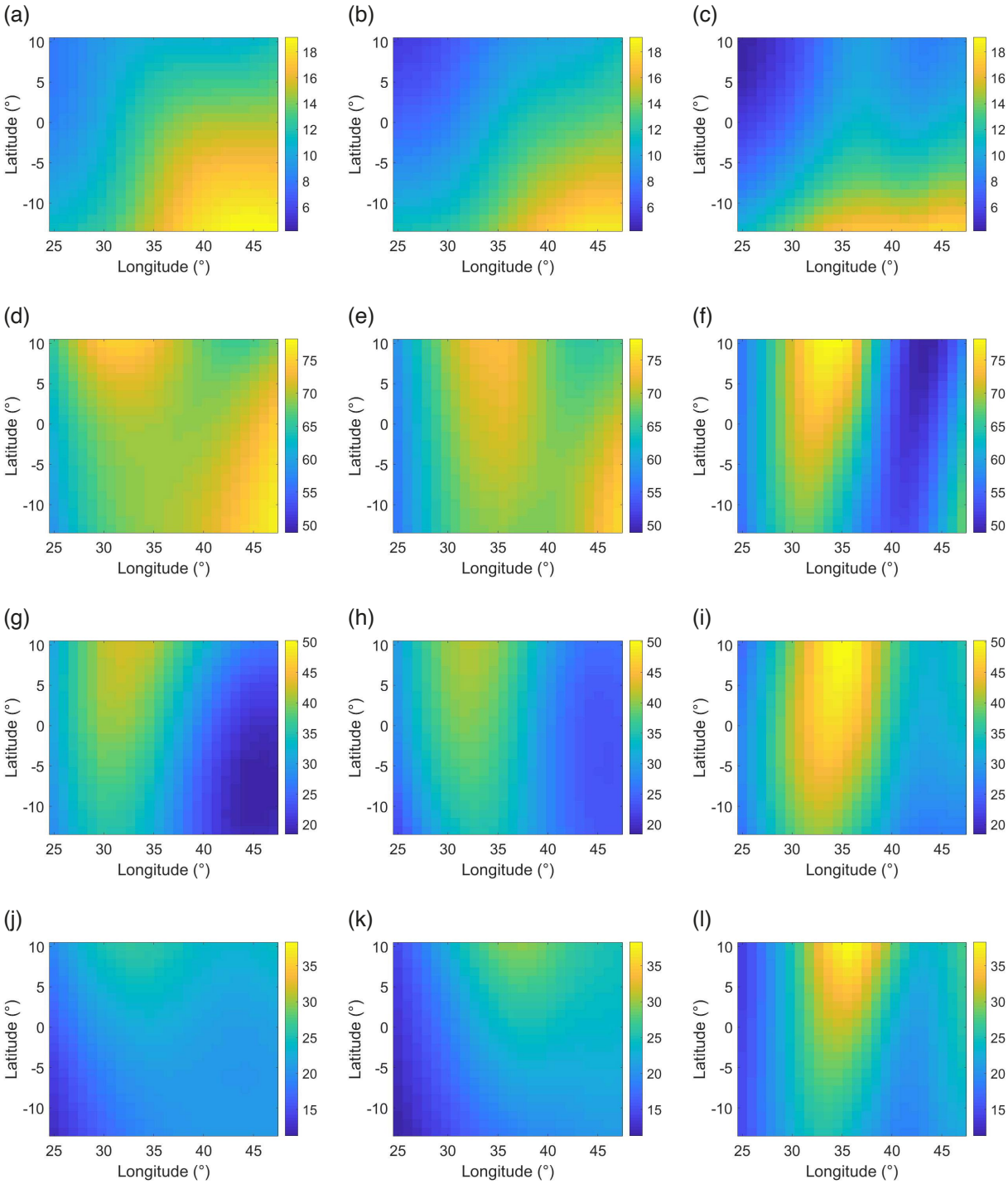

Figure 5. TEC maps (a) CODE-TEC on 25 April 2013, at 03:00 UT (disturbed day), (b) IONOLAB-Fusion-TEC on 25 April 2013, at 03:00 UT, (c) IRI-Plas-TEC on 25 April 2013, at 03:00 UT, (d) CODE-TEC on 8 April 2015, at 12:00 UT (quiet day), (e) IONOLAB-Fusion-TEC on 8 April 2015, at 12:00 UT, (f) IRI-Plas-TEC on 8 April 2015, at 12:00 UT, (g) CODE-TEC on 17 April 2011, at 18:00 UT (quiet day), (h) IONOLAB-Fusion-TEC on 17 April 2011, at 18:00 UT, (i) IRI-Plas-TEC on 17 April 2011, at 18:00 UT, (j) CODE-TEC on 24 April 2012, at 23:00 UT (disturbed day), (k) IONOLAB-Fusion-TEC on 24 April 2012, at 23:00 UT, (l) IRI-Plas-TEC on 24 April 2012, at 23:00 UT.

and 24 April 2012 (disturbed day) at 23:00 UT. In each case, the leftmost column corresponds to CODE-GIM, the middle column represents IONOLAB-Fusion-TEC, and the rightmost column shows IRI-Plas-TEC results.

In Fig. 5a, 5b and 5c, TEC values are relatively low compared to the other time periods, consistent with nighttime conditions. The IONOLAB-Fusion-TEC distribution closely reproduces the latitudinal and longitudinal gradients observed in CODE-GIM, particularly the enhancement toward the eastern sector, whereas IRI-Plas-TEC exhibits smoother variations and weaker gradients. In Fig. 5d, 5e and 5f, the TEC maps display the expected increase in TEC driven by solar ionization. The IONOLAB-Fusion-TEC map shows excellent agreement with CODE-GIM, both in magnitude and in spatial distribution. The latitudinal enhancements north and south of the magnetic equator are consistent with the formation of Equatorial Ionization Anomaly (EIA) crests. IONOLAB-Fusion successfully captures the development of these structures, while IRI-Plas-TEC underrepresents them. In Fig. 5g, 5h and 5i, TEC values begin to decrease as solar radiation weakens. The IONOLAB-Fusion-TEC results effectively reproduce both the magnitude and the westward-shifted maximum observed in CODE-GIM, whereas IRI-Plas-TEC slightly overestimates TEC during this westward shift. Finally, in Fig. 5j, 5k and 5l, overall TEC levels remain low under nighttime conditions. The IONOLAB-Fusion-TEC results maintain close agreement with CODE-GIM, accurately capturing the weak residual enhancement in the northern sector, while IRI-Plas-TEC tends to overestimate the TEC in this region.

The difference between maps can be calculated using the root mean square (RMS) method as

$$\mathrm{RMS} = \sqrt{\frac{1}{N_\theta N_\phi} \sum_{n_\theta=1}^{N_\theta} \sum_{n_\phi=1}^{N_\phi} \left(x(n_\theta, n_\phi) - \hat{x}(n_\theta, n_\phi) \right)^2}$$

where η_θ and η_ϕ represents number of latitudes and longitudes, respectively, where $1 \leq \eta_\theta \leq N_\theta$ and $1 \leq \eta_\phi \leq N_\phi$. x denotes the GIM-TEC and $\hat{x}$ represents the calculated TEC.

The RMS results for 25 April 2013, at 03:00 UT, 8 April 2015, at 12:00 UT, 17 April 2011, at 18:00 UT and 24 April 2012, at 23:00 UT are given in Table 1.

Table 1. RMS comparison of the CODE-TEC, IONOLAB-Fusion and IRI-Plas-TEC results for quiet and disturbed days at different hours.

Date and Time	RMS(TECU)	
	IONOLAB-Fusion-TEC Map	IRI-Plas-TEC Map
25 April 2013 03:00 UT	2.80	7.76
8 April 2015 12:00 UT	2.46	10.91
17 April 2011 18:00 UT	1.74	2.84
24 April 2012 23:00 UT	2.34	4.80

When the GIM-TEC data are considered as the reference, the TEC maps generated by IONOLAB-Fusion show significantly better performance than those obtained from the IRI-Plas model, achieving improvements of 77.45% on quiet days and 63.92% on disturbed days. IONOLAB-Fusion maintains good consistency with CODE-GIM, even under disturbed ionospheric conditions.

For South Africa, the region of interest spans latitudes between 20°N and 36°S and longitudes between 16°E and 20°E. The boundary of the expanded region is situated between 18°N and 38°S latitude and 10°E and 37°E longitude. The ground-based receivers are optimized with 20% sampling rate using uniform square sampling with the inclusion of augmented virtual receivers.

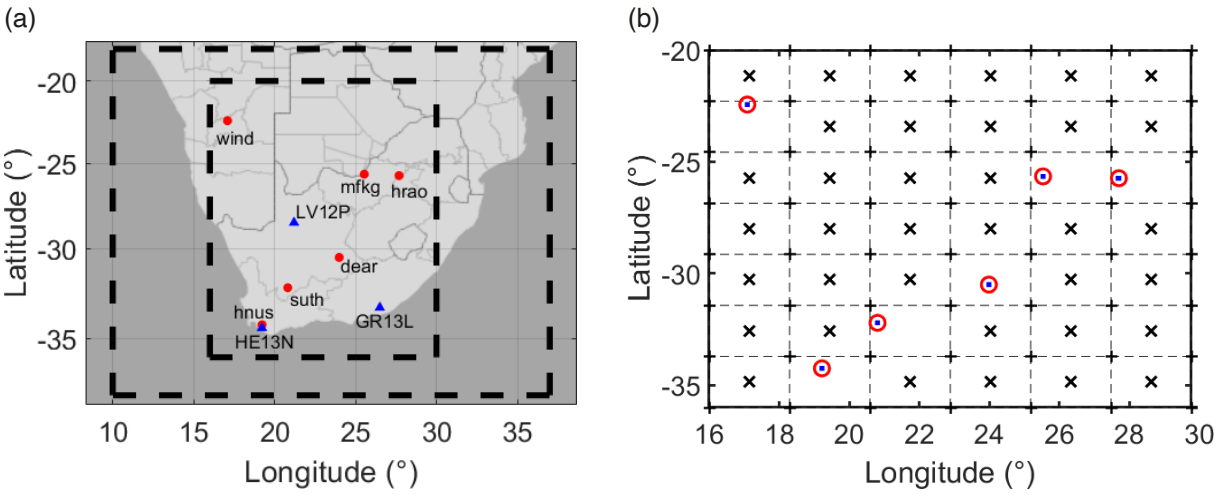

Figure 6. (a) Region of interest within the enlarged region with GPS stations indicated with (red circles, ●) and ionosondes indicated with (blue triangles, ▲), (b) The virtual ground-based receiver stations indicated with (×) and GPS stations indicated with (red circles, ●).

To validate the results obtained from IONOLAB-Fusion, the electron density values at the locations of the ionosonde stations are compared with the corresponding ionosonde vertical electron density profiles. The ionosondes utilized in this study, along with their geographical and geomagnetic coordinates and station identifiers, are listed in Table 2.

Table 2. Selected ionosonde locations in the South Africa region.

Ionosonde	Name	Geographical Coordinates		Geomagnetic Coordinates	
		Latitude (°S)	Longitude (°E)	Latitude (°S)	Longitude (°E)
HE13N	Hermanus	34.40	19.20	42.33	82.13
GR13L	Grahamstown	33.30	26.50	41.95	90.17
LV12P	Louisvale	28.50	21.20	38.31	86.87

Examples of reconstructed electron densities at the ionosonde locations are given in Fig. 7, along with ionosonde vertical electron density profiles. Electron density profiles calculated from IRI-Plas model are also illustrated in Fig. 7. Specifically, Fig. 7 presents electron density profiles for, (a) 24 April 2012 at 03:00 UT, a disturbed day at the HE13N location, (b) 17 April 2011 at 08:00 UT, a quiet day at HE13N location, (c) 8 April 2015 at 12:00 UT, a quiet day at LV12P location, and (d) 17 April 2011 at 23:00 UT, a quiet day at GR13L location.

The accuracy of the electron density reconstructions produced by IONOLAB-Fusion is assessed by comparing the reconstructed electron density profiles at the ionosonde locations with the corresponding vertical electron density profiles measured by the ionosondes. The normalized metric distance is obtained by calculating the ratio of the metric distances between two vectors to the reference vector as

$$\mathrm{NL2}(\%) = \frac{\|\underline{z}_1 - \underline{z}_2\|_2}{\|\underline{z}_1\|_2} \times 100$$

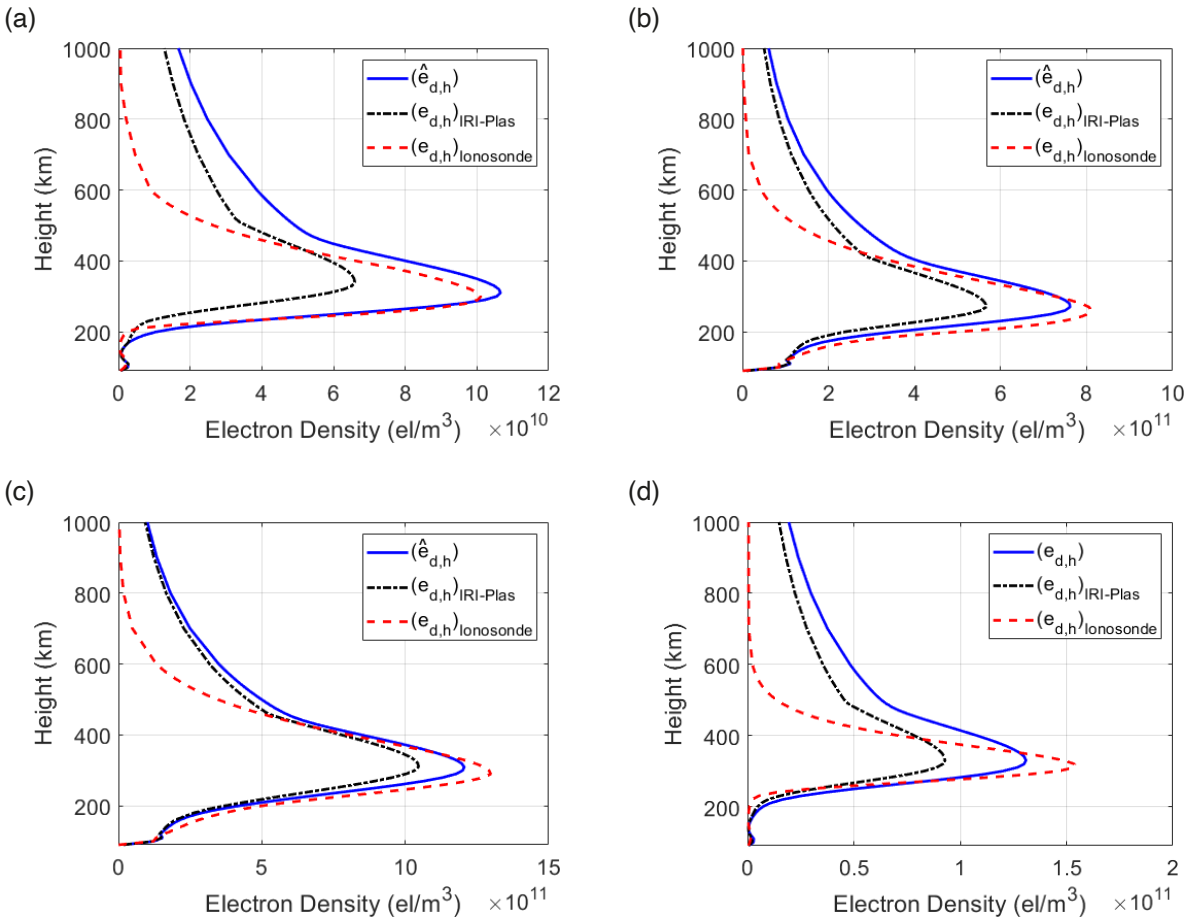

Figure 7. The reconstructed electron densities by IONOLAB-Fusion and the electron densities calculated by IRI-Plas at the location of the ionosonde vertical electron density profiles: (a) 24 April 2012 (disturbed day) at 03:00 UT, HE13N location, (b) 17 April 2011 (quiet day) at 08:00 UT, HE13N location, (c) 8 April 2015 (quiet day) at 12:00 UT, LV12P location, (d) 17 April 2011 (quiet day) at 23:00 UT, GR12L location.

Symmetric Kullback-Leibler Distance (SKLD) provides the entropical distance between two probability density functions and compares the formal similarity (Nielsen and Nock, 2009). The SKLD is calculated as

$$\mathrm{SKLD} = \sum_{n_l=1}^{N_l} z_{1,n}\,[n_l] ln\left(\frac{z_{1,n}[n_l]}{z_{2,n}[n_l]}\right) + \sum_{n_l=1}^{N_l} z_{2,n}\,[n_l] ln\left(\frac{z_{2,n}[n_l]}{z_{1,n}[n_l]}\right)$$

where and η_l represents lexicographical index and is between $1 \le \eta_l \le N_l$. $\bar{z}_n$, the empirical probability density function, is defined as

$$\underline{z}_n = \frac{1}{\sum_{n_l=1}^{N_l} z_n\,[n_l]}\underline{z}$$

The comparison is performed at different heights, including hmF2 (N_{hmF2}), Chapman (N_{chap}), and up to 1,000 km, independently. Furthermore, to evaluate the improvement of the tomography results relative to the ionospheric model, the electron density derived from the IRI-Plas model at the ionosonde locations is compared with the ionosonde measurements, which serve as reference values. The results of the comparison shown in Fig. 7 are summarized in Table 3.

Electron density reconstructions are performed using IONOLAB-Fusion for 24 April 2012 at 03:00 UT, a disturbed day at HE13N, 17 April 2011 at 08:00 UT, a quiet day at HE13N, 8 April 2015 at 12:00 UT, a quiet day at LV12P and 17 April 2011 at 23:00 UT, a quiet day at GR13L. In 24 April 2012 at 03:00 UT, a disturbed day at HE13N, 17 April 2011

Table 3. Comparison results for the date, time and ionosondes given in Fig. 7.

Date and Time	Ionosonde	Height	NL2 (%)	SKLD	$NL2_{IRI\text{-}Plas}$ (%)	$SKLD_{IRI\text{-}Plas}$
24 April 2012 03:00 UT (disturbed day)	HE13N	hmF2	9.36	7.38×10^{-2}	61.60	20.29×10^{-2}
		Chapman	13.07	3.19×10^{-2}	43.78	16.72×10^{-2}
		1,000 km	31.70	25.44×10^{-2}	44.97	46.99×10^{-2}
17 April 2011 08:00 UT (quiet day)	HE13N	hmF2	19.47	1.90×10^{-2}	41.56	4.77×10^{-2}
		Chapman	14.46	2.86×10^{-2}	32.01	4.27×10^{-2}
		1,000 km	24.75	21.54×10^{-2}	34.04	24.48×10^{-2}
8 April 2015 12:00 UT (quiet day)	LV12P	hmF2	13.57	0.97×10^{-2}	26.26	1.23×10^{-2}
		Chapman	9.41	1.11×10^{-2}	19.63	1.64×10^{-2}
		1,000 km	17.28	12.54×10^{-2}	22.24	13.80×10^{-2}
17 April 2011 23:00 UT (quiet day)	GR13L	hmF2	20.34	19.05×10^{-2}	41.02	16.03×10^{-2}
		Chapman	25.23	12.77×10^{-2}	35.20	12.43×10^{-2}
		1,000 km	50.72	65.06×10^{-2}	45.72	68.82×10^{-2}

at 08:00 UT, a quiet day at HE13N and 8 April 2015 at 12:00 UT, a quiet day at LV12P, the reconstructed electron density profiles show strong agreement with the ionosonde measurements across all altitudes, both in terms of profile shape and magnitude, and demonstrate markedly better consistency than the corresponding IRI-Plas model results. For 17 April 2011 at 23:00 UT, a disturbed day at GR13L, the IONOLAB-Fusion reconstructions perform better than the IRI-Plas model, exhibiting electron density profiles that more closely match the ionosonde vertical measurements in magnitude. The similarity in SKLD values between the IONOLAB-Fusion reconstruction and the IRI-Plas model indicates that both have comparable vertical structure up to the Chapman height. However, above this altitude, both profiles deviate from the ionosonde vertical electron density.

In this study, ray paths between ground-based receiver and GPS satellites, as well as, receivers on-board LEO satellites and GPS satellites can be modeled through the ionosphere using the IONOLAB-mRAY algorithm to construct the sampling matrix. The optimal temporal resolution between LEO and GPS satellite pairs was determined by considering the Wide Sense Stationarity (WSS) period of the midlatitude ionosphere, as described in (Arikan et al., 2018; Koroglu, 2012; Sayin et al., 2010; Yenen, 2017; Yenen and Arikan, 2024; Yenen, 2024). The WSS period represents the time interval during which the first and second moments of the experimental probability density function remain statistically constant. According to the findings reported in (Arikan et al., 2018; Koroglu, 2012; Sayin et al., 2010; Yenen, 2017; Yenen and Arikan, 2024; Yenen, 2024), the WSS period for the midlatitude ionosphere is approximately 11 minutes. Within this interval, the temporal resolution must satisfy two competing requirements, maximizing the number of available observations while ensuring that consecutive slant ray paths do not intersect the same 3-D voxels at the chosen spatial resolution. To balance these constraints and avoid voxel overlap, a temporal resolution of 30 s is adopted, allowing ray paths from different satellite pairs to sample distinct voxels (Yenen and Arikan, 2024). The paths between LEO-GPS satellite pairs within WSS period are added to the reconstruction for 17 April 2011, 23:00 UT, quiet day.

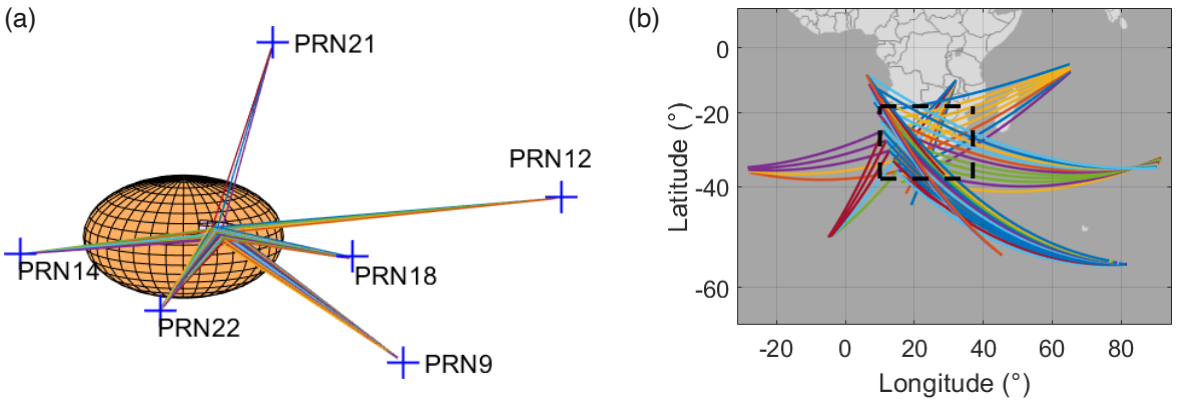

Figure 8. (a) 3-D representation of the rays between LEO and GPS satellites, (b) projection of the rays to Earth on 17 April 2011 at 23:00 UT.

The inclusion of these additional slant paths improved the estimated electron density distribution, yielding a vertical profile that more closely aligned with the ionosonde-derived electron density at the GR13L location, as illustrated in Fig. 9.

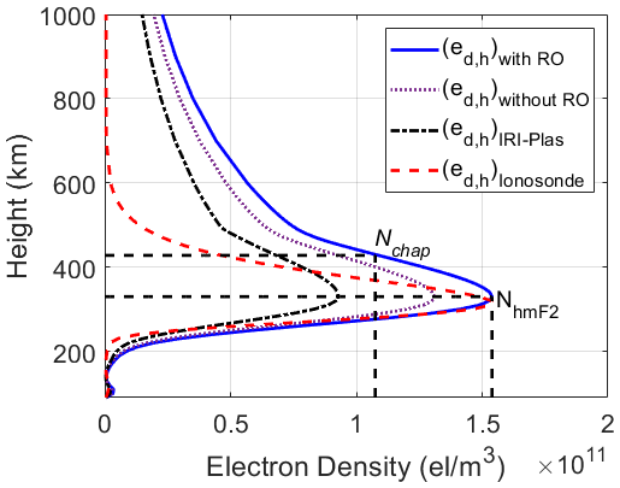

Figure 9. The reconstructed electron densities by IONOLAB-Fusion using rays between LEO and GPS satellites and the electron densities calculated by IRI-Plas at the location of the ionosonde vertical electron density profiles 17 April 2011 (quiet day) at 23:00 UT, GR12L location.

The similarity between the ionosonde-derived vertical electron density profile and the reconstructed electron density at the GR13L location, both without and with the inclusion of slant paths, is evaluated using the NL2 and SKLD metrics. Additionally, the similarity between the ionosonde vertical electron density profile and the IRI-Plas vertical electron density profile is analyzed to serve as a reference for comparison. The similarity in SKLD values between the electron density reconstructed by IONOLAB-Fusion and that calculated by the IRI-Plas model indicates that both approaches reproduce a comparable vertical structure of the ionosphere up to the Chapman height. However, beyond this altitude, the IONOLAB-Fusion reconstruction maintains better consistency with the ionosonde profile, demonstrating its superior capability in capturing the upper ionospheric electron density distribution.

It is observed that, both without and with the inclusion of slant ray paths, the IONOLAB-Fusion reconstructions exhibit substantially closer agreement with the ionosonde-derived vertical electron density profiles than those obtained from the IRI-Plas model. Quantitatively, improvements of 50.41% without RO and 54.49% with RO are achieved up to the hmF2 height, and 28.32% and 8.47% are obtained up to the Chapman height, respectively. These results demonstrate that IONOLAB-Fusion significantly outperforms the background ionospheric model in

Table 4. Comparison results for 17 April 2011 (a quiet day) at 23:00 UT are presented for IONOLAB-Fusion reconstructions obtained with and without the inclusion of RO data. The corresponding comparison for the IRI-Plas model is also provided as a reference.

Date and Time	Ionosonde	Height	Without RO				With RO	
			NL2 (%)	SKLD	$NL2_{IRI\text{-}Plas}$ (%)	$SKLD_{IRI\text{-}Plas}$	NL2 (%)	SKLD
17 April 2011 23:00 UT (quiet day)	GR13L	hmF2	20.34	19.05×10^{-2}	41.02	16.03×10^{-2}	18.51	19.05×10^{-2}
		Chapman	25.23	12.77×10^{-2}	35.20	12.43×10^{-2}	32.22	12.77×10^{-2}
		1,000 km	50.72	65.06×10^{-2}	45.72	68.82×10^{-2}	61.66	65.06×10

reproducing the bottomside ionosphere, where ionosonde measurements provide reliable ground truth. Above these altitudes, both reconstructed profiles begin to deviate from the ionosonde measurements. This behavior is expected, since ionosondes do not provide direct measurements beyond the hmF2 peak, and the topside ionosphere and plasmasphere are reconstructed based on the underlying physical assumptions and inversion strategies embedded in the respective models (Gok et al., 2022). Consequently, discrepancies at higher altitudes primarily reflect differences in the physical modeling of the topside ionosphere rather than limitations of the reconstruction algorithm itself. Since IONOLAB-Fusion incorporates the IRI-Plas model as its background ionosphere, the SKLD values exhibit nearly identical results, with only minimal numerical differences, regardless of whether slant ray paths between LEO-based and GPS satellites are included. This behavior indicates that the overall shape similarity between reconstructed and reference profiles is already well constrained by the physically consistent background model. Nevertheless, the inclusion of slant ray paths provides additional observational constraints, particularly in the bottomside ionosphere, leading to improved NL2 performance and enhanced agreement with ionosonde measurements. Overall, these results demonstrate that the inclusion of slant ray paths improves the reconstruction accuracy primarily up to the hmF2 peak, where ionosonde observations are available and most reliable. This confirms that RO-supported slant ray geometry contributes most effectively to refining the bottomside electron density distribution, yielding reconstructed profiles that more closely correspond to ionosonde-derived electron densities.

In this study, a comparative evaluation of IONOLAB-Fusion against established ionospheric reconstruction techniques is also presented. For the South Africa region, electron density reconstructions obtained using IONOLAB-Fusion are compared with results derived from Spherical Cap Harmonics, Haar Wavelets, B-Spline and Slepian function basis representations. For the selected set of dates, times, and ionosonde stations under quiet ionospheric conditions, namely 17 April 2011 at 08:00 UT for the HE13N station, 8 April 2015 at 12:00 UT for the LV12P station, and 17 April 2011 at 23:00 UT for the GR13L station, the electron density reconstruction results obtained using IONOLAB-Fusion (Y1), Spherical Cap Harmonics (Y2), Haar Wavelets (Y3), B-Spline functions (Y4), and Slepian functions (Y5) are compared with ionosonde vertical electron density profiles, which are taken as ground truth. All available ionosonde profiles and corresponding reconstruction results across the selected dates and times are combined into a single dataset, and the NL2 and SKLD metrics are computed collectively up to the hmF2 height, Chapman height, and 1,000 km altitude. In parallel, electron density profiles obtained from the IRI-Plas model are also compared with the ionosonde measurements, and the resulting comparison metrics are used as reference values.

Figure 10 presents a quantitative comparison of electron density reconstructions obtained using five tomography techniques against ionosonde vertical profiles for three quiet-day cases. The NL2 comparison results evaluated up to the hmF2 height, the Chapman peak height, and 1,000 km for each reconstruction method as well as for the IRI-Plas model are presented in Fig. 10a, 10c, and 10e. The corresponding SKLD results up to the hmF2 height, the Chapman peak height, and 1,000 km are shown in Fig. 10b, 10d, and 10f.

Figure 10 presents a quantitative comparison of electron density reconstruction performance for five different tomography techniques: IONOLAB-Fusion (Y1), Spherical Cap Harmonics (Y2), Haar Wavelets (Y3), B-Spline

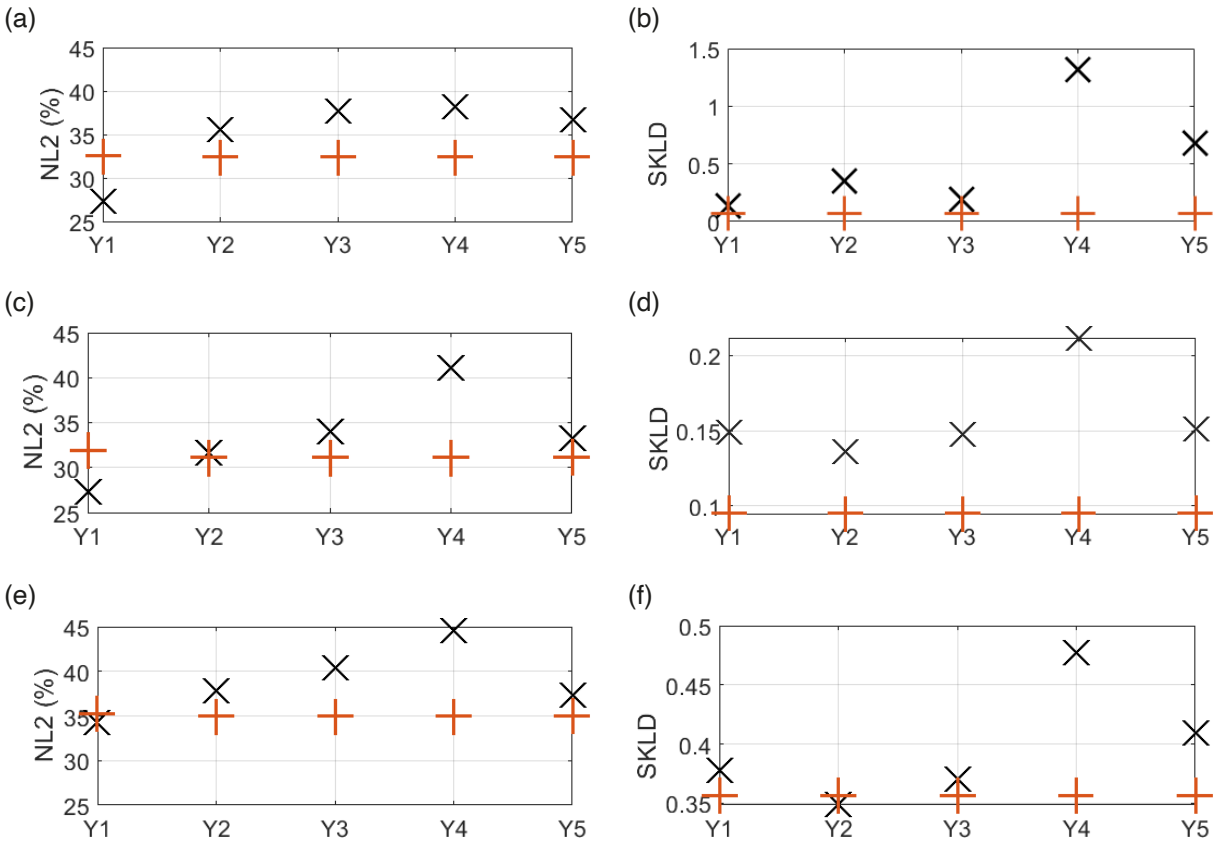

Figure 10. Comparison results of electron density reconstructions obtained using five tomography techniques against ionosonde vertical profiles for all selected quiet day cases. Reconstruction methods include IONOLAB-Fusion (Y1), Spherical Cap Harmonics (Y2), Haar Wavelets (Y3), B-Spline functions (Y4), and Slepian functions (Y5). Panel (a) presents the NL2 results up to hmF2, (b) the corresponding SKLD results up to hmF2, (c) the NL2 results up to the Chapman peak height, (d) the corresponding SKLD results up to the Chapman peak height, (e) the NL2 results up to 1000 km, and (f) the corresponding SKLD results up to 1000 km. Comparisons between reconstruction methods and ionosonde profiles are indicated by (×), while comparisons between IRI-Plas electron density profiles and ionosonde measurements are indicated by (+).

functions (Y4), and Slepian functions (Y5), using ionosonde vertical profiles as ground truth. The normalized NL2 and SKLD metrics are evaluated up to the hmF2 peak, Chapman height, and 1,000 km for three quiet-day cases. Across all test cases and altitude ranges, IONOLAB-Fusion (Y1) consistently yields the lowest NL2 and SKLD values, indicating the closest agreement with ionosonde measurements in both magnitude and profile shape. This demonstrates the superior reconstruction capability of IONOLAB-Fusion relative to the alternative basis function approaches. The Spherical Cap Harmonics (Y2) and Haar Wavelets (Y3) exhibit moderate performance, with larger NL2 and SKLD values, reflecting increased deviations in both electron density magnitude and vertical profile structure. The B-Spline method (Y4) consistently produces the highest errors across all cases, particularly evident in the Chapman and 1,000 km altitude ranges, indicating reduced stability and sensitivity to sparse ray-path geometry. The Slepian function approach (Y5) performs better than B-Splines but remains less accurate than IONOLAB-Fusion. The comparison with IRI-Plas indicates that, although IRI-Plas provides a reasonable background model, its agreement with ionosonde measurements is systematically weaker than that of IONOLAB-Fusion for all cases and altitude ranges in terms of the NL2 metric, with similar behavior observed for the SKLD metric. This highlights the advantage of data-driven tomographic reconstruction over empirical background modeling.

Overall, Fig. 10 confirms that IONOLAB-Fusion provides the most accurate and robust reconstruction of ionospheric electron density profiles among the tested methods, both in terms of magnitude and shape similarity, under quiet ionospheric conditions.

The Turkish National Permanent GPS Network (TNPGN-Active) consists of 146 continuously operating GPS stations uniformly distributed across Türkiye and the Turkish Republic of Northern Cyprus. The distance between the

receiver stations in the TNPGN-Active GPS network varies between 80 and 100 km. In the study by (Deviren et al., 2013; Koroglu, 2012; Yenen, 2017), the TNPGN-Active GPS network was divided into 19 subregions with 2° × 3° in latitude and longitude to facilitate data analysis and the application of statistical methods. These subregions are denoted by the parameter *R*. The stations located at the centers of the subregions, which are approximately equidistant from other stations within the same region, are selected as the reference stations of the respective regions (Yenen, 2017).

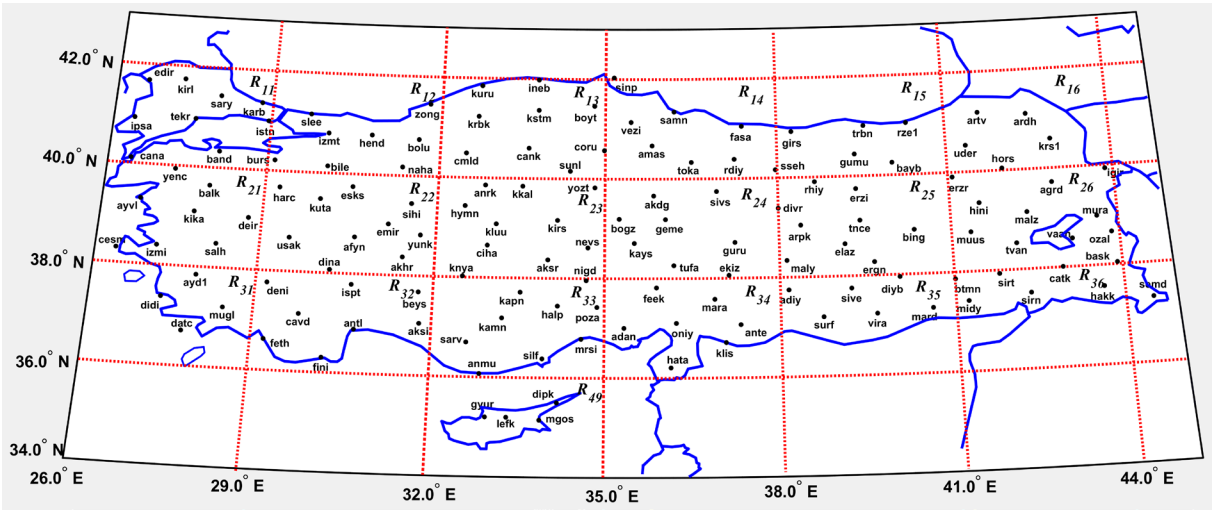

Figure 11. TNPGA-Active GPS network (Koroglu, 2012).

In this study, electron density reconstruction is performed for the Türkiye region, extending from 36°N to 42°N latitude and 26°E to 45°E longitude. The reconstruction utilized reference GPS stations from the TNPGN-Active network. The ionosphere is discretized into three-dimensional voxels, with spatial resolutions optimized according to the limitations of the IRI-Plas model, using 1° in latitude and 1° in longitude. The vertical resolution is defined as 10 km between 90 km and 600 km, and 100 km between 600 km and 1,000 km. For the Türkiye region, the ionosphere is reconstructed up to 1,000 km, as TEC contributions above this altitude vary by less than approximately 3 TECU in the midlatitude region. This height limitation reduces measurement complexity and computational burden while preserving reconstruction accuracy, demonstrating the algorithm's adaptability to regional ionospheric characteristics.

The model matrix is generated using electron density values computed three days prior to the reconstruction period, a configuration selected through the GUI to enhance temporal stability and consistency.

In Fig. 12, we present slice representations of electron density reconstructions within the selected region of the ionosphere for both quiet and disturbed days at different times, displayed in the leftmost column. The middle column shows electron densities calculated using the IRI-Plas model for the same dates and times. The rightmost column depicts the differences between the electron density reconstructions and the densities calculated from the IRI-Plas model. The reconstruction results utilized only the ground-based receivers in the IONOLAB-Fusion algorithm. In Fig. 12a, 12d, 12g, 12j and 12m electron density is reconstructed for 8 April 2015 ionospheric quiet day for 03:00 UT, 08:00 UT, 12:00 UT, 18:00 UT and 23:00 UT, respectively. The slice heights are selected between 100 km and 500 km with a resolution of 100 km.

Figure 12a presents the reconstructed electron density distribution for 8 April 2015 at 03:00 UT. During nighttime hours, ionization levels are low, with the maximum electron density observed around 300 km altitude in the southeastern part of the region. Figure 12d shows the distribution for 8 April 2015 at 08:00 UT, when the ionosphere begins to ionize as the Sun rises, leading to a gradual increase in electron density. The eastern portion of the region exhibits higher values due to earlier solar illumination, with the most pronounced electron density still located near 300 km, while lower altitudes also begin to ionize. In Fig. 12g, corresponding to 12:00 UT, the peak electron density remains near 300 km, but the enhancement becomes more spatially uniform, extending across the entire region. Figure 12j depicts the electron density at 18:00 UT, when the Sun sets over the western horizon. At this time, the highest electron density is still observed near 300 km, particularly over the western part of the region due to the

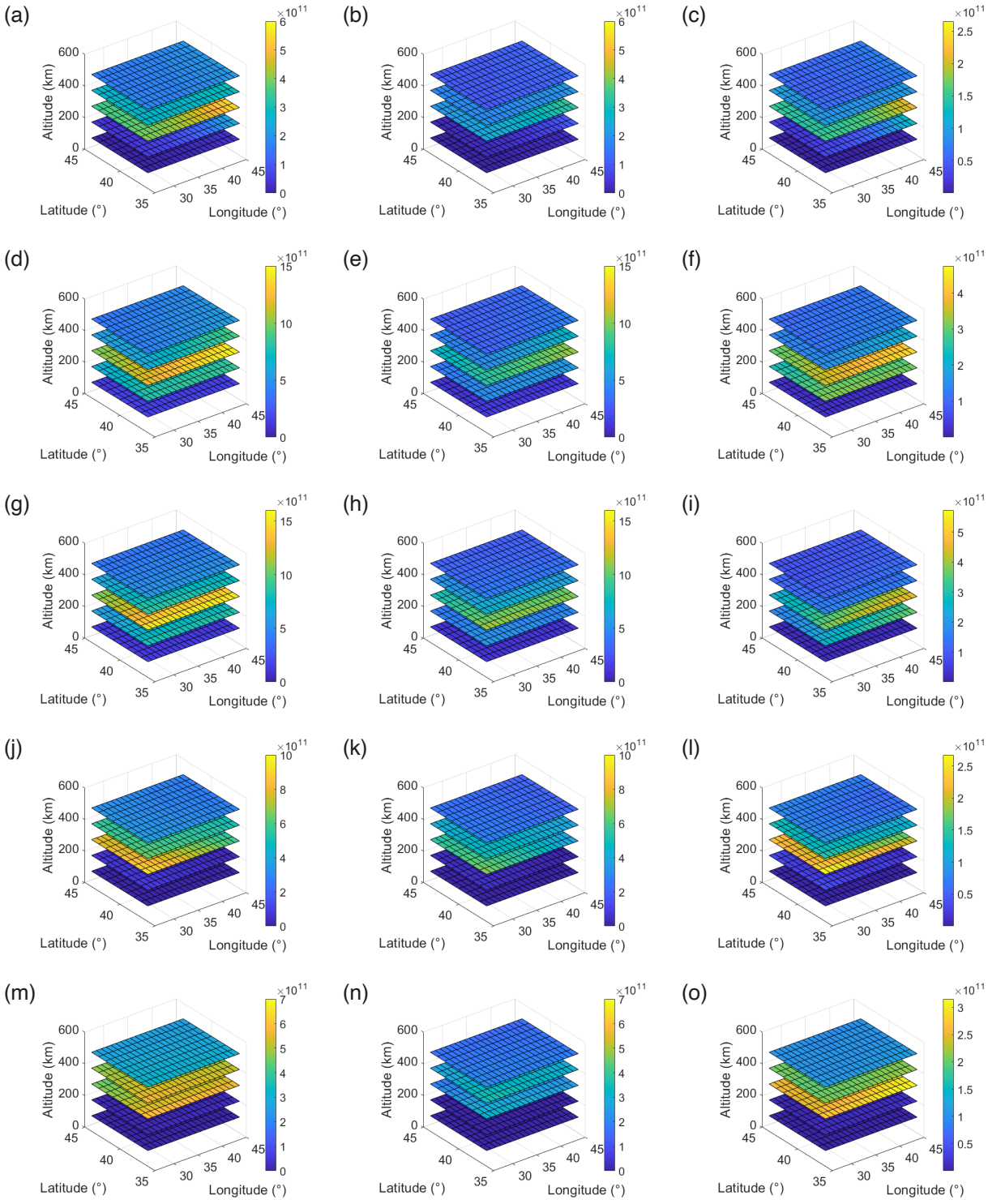

Figure 12. Slices of electron densities with 100 km resolution for different dates and times: (a) reconstructed using IONOLAB-Fusion on 8 April 2015, at 03:00 UT (quiet day), (b) calculated by IRI-Plas on 8 April 2015, at 03:00 UT, (c) the difference between IONOLAB-Fusion and IRI-Plas for 8 April 2015, at 03:00 UT, (d) reconstructed using IONOLAB-Fusion on 8 April 2015, at 08:00 UT (quiet day), (e) calculated by IRI-Plas on 8 April 2015, at 08:00 UT, (f) the difference between IONOLAB-Fusion and IRI-Plas for 8 April 2015, at 08:00 UT, (g) reconstructed using IONOLAB-Fusion on 8 April 2015, at 12:00 UT (quiet day), (h) calculated by IRI-Plas on 8 April 2015, at 12:00 UT, (i) the difference between IONOLAB-Fusion and IRI-Plas for 8 April 2015, at 12:00 UT, (j) reconstructed using IONOLAB-Fusion on 8 April 2015, at 18:00 UT (quiet day), (k) calculated by IRI-Plas on 8 April 2015, at 18:00 UT, (l) the difference between IONOLAB-Fusion and IRI-Plas for 8 April 2015, at 18:00 UT, (m) reconstructed using IONOLAB-Fusion on 8 April 2015, at 23:00 UT (quiet day), (n) calculated by IRI-Plas on 8 April 2015, at 23:00 UT, (o) the difference between IONOLAB-Fusion and IRI-Plas for 8 April 2015, at 23:00 UT.

sunset. Finally, Fig. 12m shows the distribution for 8 April 2015 at 23:00 UT. As ionization depends on solar radiation, a general decrease in electron density is observed after sunset at all altitudes. However, compared to 03:00 UT, the electron density remains relatively elevated at 300-400 km, reflecting the cumulative effect of solar radiation throughout the day. From Fig. 12c, 12f, 12i, 12l, and 12o, it can be observed that IRI-Plas tends to underestimate the electron density during quiet-day conditions.

Figure 13 presents TEC maps derived from CODE-GIM, IONOLAB-Fusion-TEC, and IRI-Plas-TEC for 8 April 2015, representing a quiet ionospheric day, at five different times of the day. IONOLAB-Fusion-TEC values are calculated from Fig. 13 using the IRI-Plas-STEC algorithm. In each case, the leftmost column corresponds to CODE-GIM, the middle column represents IONOLAB-Fusion-TEC, and the rightmost column shows IRI-Plas-TEC results.

In Fig. 13a, 13b and 13c, during the nighttime period TEC values remain low, consistent with reduced ionization levels in the absence of solar radiation. The IONOLAB-Fusion-TEC map closely follows the spatial gradient and overall structure observed in CODE-GIM, whereas IRI-Plas-TEC underestimates the TEC magnitude. In Fig. 13d, 13e and 13f, as aytime ionization increases after sunrise, all TEC maps show a noticeable rise in TEC value. The IONOLAB-Fusion-TEC results once again demonstrate strong consistency with CODE-GIM, while IRI-Plas-TEC continues to yield lower TEC values and weaker gradients. In Fig. 13g, 13h and 13i, at local noon, TEC values reach their maximum as solar radiation peaks. Both CODE-GIM and IONOLAB-Fusion-TEC maps exhibit similar spatial distribution and values, indicating great agreement in representing daytime ionospheric conditions. In contrast, IRI-Plas-TEC underestimates the TEC peak. In Fig. 13j, 13k and 13l, toward sunset, TEC begins to decline. IONOLAB-Fusion-TEC maintains close correspondence with CODE-GIM, accurately reproducing the overall magnitude and horizontal gradients. The IRI-Plas-TEC map, however, continues to show lower TEC values. In Fig. 13m, 13n and 13o, under nighttime conditions, TEC levels decrease uniformly across the region. The IONOLAB-Fusion-TEC distribution remains in good accordance with CODE-GIM while IRI-Plas-TEC underestimating TEC throughout the domain.

The quantitative comparison between CODE-TEC values and the TECs obtained from IONOLAB-Fusion and IRI-Plas reconstructions for 8 April 2015 is presented in Table 5.

Table 5. RMS comparison of the CODE-TEC, IONOLAB-Fusion and IRI-Plas-TEC results for Türkiye on 8 April 2015 (quiet day) at different times, throughout the day.

Time	RMS (TECU)	
	IONOLAB-Fusion-TEC Map	IRI-Plas-TEC Map
03:00 UT	0.55	5.77
08:00 UT	1.24	10.88
12:00 UT	1.74	11.06
18:00 UT	1.39	5.07
23:00 UT	1.02	7.31

When the GIM-TEC data are considered as the reference, the TEC maps generated by IONOLAB-Fusion show significantly better performance than those obtained from the IRI-Plas model, achieving improvements of 90.47% even though the full ionospheric and plasmaspheric region up to the GPS satellite altitude was not utilized.

From a computational perspective, the processing time of IONOLAB-Fusion depends on the user-defined latitude, longitude, and height ranges, as well as the selected spatial resolutions. The most computationally intensive step is the generation of the model matrix; however, once created, the matrix can be stored and reused for subsequent reconstructions, substantially reducing computational overhead. On a system equipped with an Intel® Core™ i5-10210U CPU at 1.60 GHz and 8 GB of RAM, a three-dimensional spherical voxel grid comprising 25 latitude, 36 longitude, and 62 height steps requires approximately one minute to reconstruct for a single-day case.

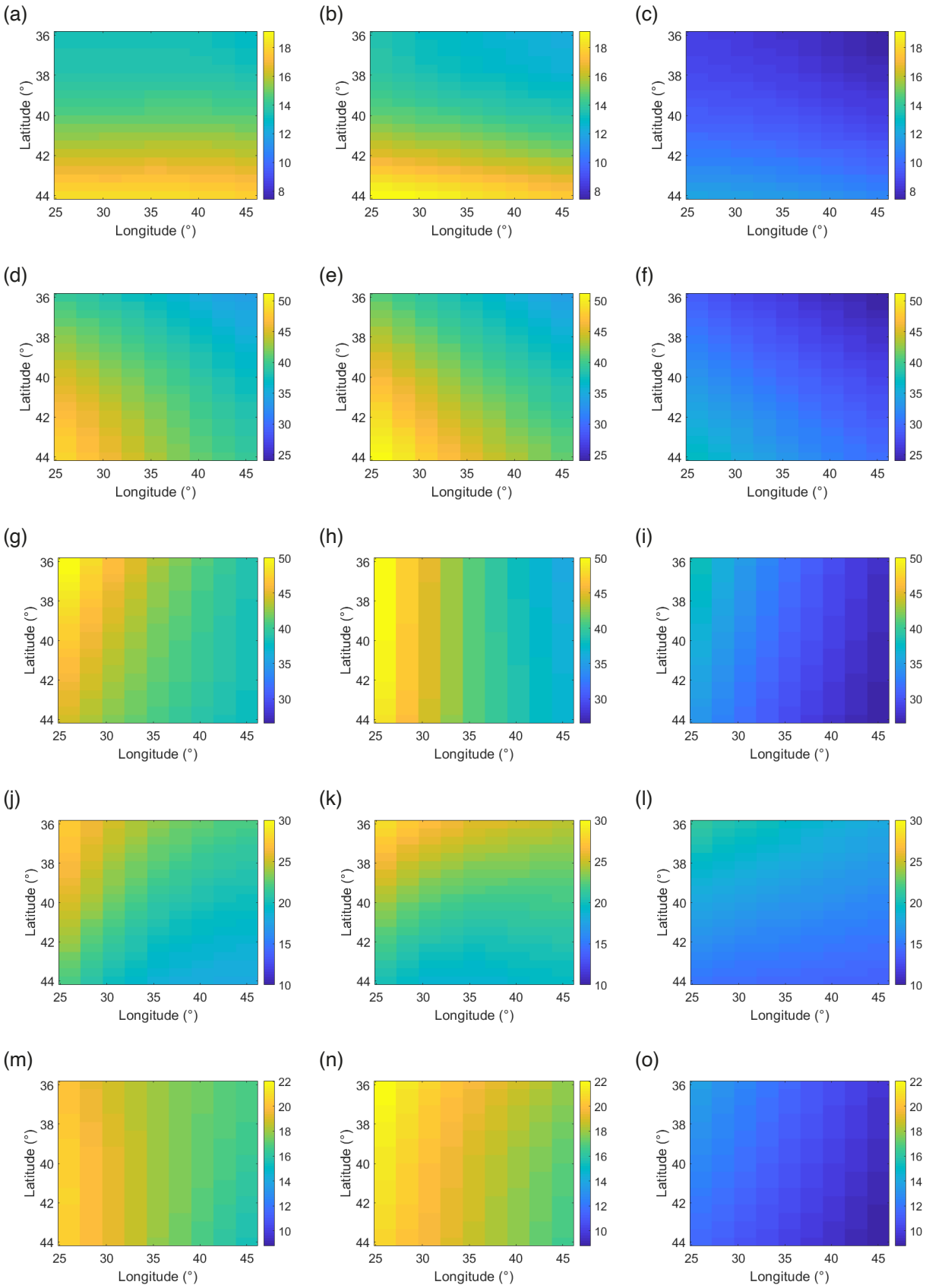

Figure 13. TEC maps for 8 April 2015, obtained from, (a) CODE-TEC at 03:00 UT (disturbed day), (b) IONOLAB-Fusion-TEC at 03:00 UT, (c) IRI-Plas-TEC at 03:00 UT, (d) CODE-TEC at 08:00 UT, (e) IONOLAB-Fusion-TEC at 08:00 UT, (f) IRI-Plas-TEC at 08:00 UT, (g) CODE-TEC at 12:00 UT, (h) IONOLAB-Fusion-TEC at 12:00 UT, (i) IRI-Plas-TEC at 12:00 UT, (j) CODE-TEC at 18:00 UT, (k) IONOLAB-Fusion-TEC at 18:00 UT, (l) IRI-Plas-TEC at 18:00 UT, (m) CODE-TEC at 23:00 UT, (n) IONOLAB-Fusion-TEC at 23:00 UT, (o) IRI-Plas-TEC at 23:00 UT.

While IONOLAB-Fusion is currently implemented as an academic research framework, adaptation to GPU-based architecture is expected to significantly reduce computation time, enabling real-time or near-real-time operation for space-weather applications (Kacar, 2018).

The IONOLAB-Fusion algorithm offers a highly flexible and reliable framework for estimating and updating ionospheric electron density profiles. Its straightforward implementation, strong agreement with ionosonde and GIM-TEC observations, and consistent performance across different geographic regions and ionospheric conditions demonstrate both its robustness and adaptability. Incorporating virtual rays within the WSS period of the ionosphere further improves reconstruction accuracy, yielding results that align more closely with ionosonde and GIM-TEC data. The findings obtained for Kenya, South Africa and Türkiye, together with the results previously reported for Europe (Yenen and Arikan, 2024), confirm that IONOLAB-Fusion is a robust and globally applicable framework for reconstructing ionospheric electron density under any regional, temporal, or geophysical condition.

4. Conclusions

This study demonstrates the effectiveness and adaptability of the IONOLAB-Fusion algorithm for reconstructing ionospheric electron density across diverse geospatial regions with varying levels of observational infrastructure. The algorithm is applied to three geographically distinct regions, Kenya, South Africa and Türkiye, representing equatorial, southern midlatitude, and northern midlatitude domains, respectively. The results confirm that IONOLAB-Fusion reliably reconstructs the spatial and temporal variability of the ionosphere under both quiet and disturbed conditions, maintaining close agreement with TEC values from CODE-GIM and ionosonde measurements.

In addition, this study presents IONOLAB-Fusion as a comprehensive and user-oriented 4-D computerized ionospheric tomography framework, in which the integration of a GUI constitutes a major methodological contribution. The GUI provides a unified and transparent operational environment that allows users to define spatial and temporal reconstruction domains, configure vertical resolution schemes, select and augment receiver networks, visualize ray geometries, and manage model matrix generation and reuse. By translating complex tomographic procedures into an intuitive and repeatable workflow, the GUI significantly enhances usability and reproducibility while preserving scientific rigor, enabling consistent application of IONOLAB-Fusion across regions with diverse ionospheric characteristics and observational constraints.

In the Kenya region, which is strongly influenced by the Equatorial Ionization Anomaly (EIA), reconstructions are performed using virtual ground-based receivers. These virtual receivers are uniformly distributed to ensure balanced spatial sampling, and model matrices are generated using Moderate Solar Activity (MSA) years that included both quiet and disturbed ionospheric conditions. In the absence of ionosonde data, the reconstructed results are validated through comparison with GIM-derived TEC maps. The RMS differences between IONOLAB-Fusion-TEC and GIM-TEC are 1.74 TECU on quiet days and 2.34 TECU on disturbed days, corresponding to improvements of 77.45% and 63.92%, respectively, over the IRI-Plas model.

For the South Africa region, the model matrix is again generated using MSA years, with tomography performed using a combination of real and virtual ground-based receivers to achieve a uniform spatial distribution. The reconstructed electron density profiles are validated against ionosonde observations at multiple stations. Excellent agreement is obtained up to the peak ionization (hmF2) and Chapman heights, with correlation metrics reaching NL2 = 9.41% and SKLD = 0.97×10^{-2} using only ground and virtual receivers. Even during disturbed conditions, the reconstructed profiles achieved up to 70% improvement in normalized metric distance relative to IRI-Plas. When slant ray paths between LEO and GPS satellites are included, IONOLAB-Fusion outperformed IRI-Plas by up to 54.49% at hmF2 altitude.

In this study, IONOLAB-Fusion algorithm was compared with electron density reconstruction results obtained using methods, including Spherical Cap Harmonics, Haar Wavelets, B-Spline functions, and Slepian functions, using ionosonde vertical electron density profiles as ground truth over South Africa under quiet ionospheric conditions. It is found that IONOLAB-Fusion outperforms these approaches by 23.25% to 28.24% up to the hmF2 altitude, demonstrating its superior reconstruction accuracy.

In the Türkiye region, the model matrix is generated retrospectively using electron density data from the three days preceding the reconstruction period. Owing to Türkiye's dense GPS network, reconstructions are performed using reference stations from subregions of the TNPGN-Active network, providing a high-resolution dataset representative of midlatitude ionospheric behavior. In the absence of ionosondes, validation is performed through comparison of

IONOLAB-Fusion-TEC with CODE-GIM TEC maps. Throughout the day, IONOLAB-Fusion consistently reproduced GIM-TEC values and outperformed the IRI-Plas model up to 90.47%.

The IONOLAB-Fusion algorithm can be readily applied to filtering, smoothing, updating, nowcasting, and forecasting tasks, offering both flexibility and operational efficiency. Although IONOLAB-Fusion has been developed as an academic research framework, adapting it to GPU-based architectures would substantially reduce computation time, enabling real-time or near-real-time reconstructions and broadening its potential for operational space-weather applications.

Overall, IONOLAB-Fusion provides a state-of-the-art, user-friendly, and scientifically rigorous computerized ionospheric tomography framework using both actual and virtual augmented ray paths. In this study, it has been demonstrated that IONOLAB-Fusion can be confidently applied to any region and ionospheric condition, providing accurate, robust, reliable, and cost-effective tomographic reconstructions of ionospheric electron density. Furthermore, the post-reconstruction electron density profiles can be incorporated into the model matrix to refine future reconstructions, enabling continuous model improvement.

Data availability statement. The datasets generated and analyzed during this study are available from the corresponding author upon request but are not publicly accessible as they will be included in future publications.

Acknowledgements. We would like to thank Esra Erdem, the developer of IONOLAB-RAY algorithm, Hakan Tuna, the developer of IONOLAB-CIT and IRI-Plas-STEC and Furkan Ardıç, for his valuable study on the categorization of years between 1999 and 2022 based on SSN and F10.7. The IONOLAB-STEC and IRI-Plas-STEC tools were accessed through the IONOLAB Space Weather Service (www.ionolab.org). The GIM-TEC data used in this study were obtained from the Center for Orbit Determination in Europe (CODE) via the IGS data archive (ftp://cddis.gsfc.nasa.gov/pub/gps/products/ionex/).

References

Al-Franek, O. J. S. (2013). Ionospheric imaging for Canadian polar regions, Doctoral Dissertation, University of Calgary, Canada.

Amerian, Y., B. Voosoghi and A. Ghaffari (2010). Tomographic reconstruction of the ionospheric electron density in term of wavelets, J. Aerospace Sci. Tech., 7, 19-29.

Ardic, F. (2023). 2-D reconstruction of total electron content using singular value decomposition, Master's Thesis, Hacettepe University, Türkiye.

Arikan, F., C. B. Erol and O. Arikan (2003). Regularized estimation of vertical total electron content from Global Positioning System data, J. Geophys. Res.: Space Phys., 108, doi:10.1029/2002JA009605.

Arikan, F., C. B. Erol and O. Arikan (2004). Regularized estimation of vertical total electron content from GPS data for a desired time period, Radio Sci., 39, 1-10, doi:10.1029/2004RS003061.

Arikan, O., F. Arikan and C. B. Erol (2007). 3-D Computerized ionospheric tomography with random field priors. In Mathematical Methods in Engineering, Springer, 325-334.

Arikan, O., F. Arikan and C. B. Erol (2007). Computerized ionospheric tomography with the IRI model, Adv. Space Res., 39, 859-866, doi:10.1016/j.asr.2007.02.078.

Arikan, F., H. Nayir, U. Sezen and O. Arikan (2008) Estimation of single station interfrequency receiver bias using GPS-TEC, Radio Sci., 43, 1-13, doi:10.1029/2007RS003785.

Arikan, F., S, Shukurov, H. Tuna, O. Arikan and T.L. Gulyaeva (2016). Performance of GPS slant total electron content and IRI-Plas-STEC for days with ionospheric disturbance, Geod. Geodyn., 7, 1, 1-10.

Arikan, F., O. Koroglu and S. D. Yenen (2018). Wide Sense Stationarity Period of Slant and Vertical Total Electron Content in Determination of Temporal Correlation of Midlatitude Ionosphere, 42nd COSPAR Scientific Assembly, Los Angeles, USA.

Austen, J. R., S. J. Franke and C. Liu (1988). Ionospheric imaging using computerized tomography, Radio Sci., 23, 299-307, doi:10.1029/RS023i003p00299.

Bust, G. S. and C. N. Mitchell (2008). History, current state, and future directions of ionospheric imaging, Rev. Geophys., 46, doi:10.1029/2006RG000212.

Deviren, M. N, F. Arikan and O. Arikan (2013). Spatio-temporal interpolation of total electron content using a GPS network, Radio Sci., 48, 3, 302-309, doi:10.1002/rds.20036.

Erdem, E., F. Arikan, M. N. Deviren and I. Cor (2015). A model based ray tracing algorithm for anisotropic and inhomogeneous ionosphere with GIM-TEC assimilation. In Proceedings of the 2015 7th International Conference on Recent Advances in Space Technologies (RAST).

Erdem, E. and F. Arikan (2017). IONOLAB-RAY: A wave propagation algorithm for anisotropic and inhomogeneous ionosphere, Turkish J. Electr. Engin. Compu. Sci., 25, 1712-1723, doi:10.3906/elk-1602-119.

Erdem, E. (2017). Electromagnetic wave propagation model and simulation in ionosphere, Doctoral Dissertation, Hacettepe University, Türkiye.

Erdem, E. and F. Arikan (2018). Communication Parameters Derived from IONOLAB-RAY Algorithm. 42nd COSPAR Scientific Assembly.

Erturk, O., O. Arikan and F. Arikan (2009). Tomographic reconstruction of the ionospheric electron density as a function of space and time, Adv. Space Res., 43, 1702-1710, doi:10.1016/j.asr.2008.08.018.

Farzaneh, S. and E. Forootan (2018). Reconstructing regional ionospheric electron density: a combined spherical Slepian function and empirical orthogonal function approach, Surv. Geophys., 39, 289-309, doi:10.1007/s10712-017-9446-y.

Feltens, J. (2003). The international GPS service (IGS) ionosphere working group, Adv. Space Res., 31, 635-644, doi:10.1016/S0273-1177(03)00029-2.

Garcia, R. and F. Crespon (2008). Radio tomography of the ionosphere: Analysis of an underdetermined, ill-posed inverse problem, and regional application, Radio Sci., 43, 1-13, doi:10.1029/2007RS003714.

Gok, G., Y. K. Alp and O. Arikan (2022). A method for automatic scaling of ionograms and electron density reconstruction, IEEE Trans. Geosci. Remote Sensing, 60, 1-11, doi:10.1109/TGRS.2021.3121621.

Gulyaeva, T., F. Arikan, U. Sezen and L. Poustovalova (2018). Eight proxy indices of solar activity for the International Reference Ionosphere and Plasmasphere model, J. Atmo. Solar-Terr. Phys., 172, 122-128, doi:10.1016/j.jastp.2018.03.025.

Jin, S. and D. Li (2018), 3-D ionospheric tomography from dense GNSS observations based on an improved two-step iterative algorithm, Adv. Space Res., 62, 809-820, doi:10.1016/j.asr.2018.05.032.

Kacar, A. (2018). GPU parallel computing of ray tracing algorithms for modeling wave propagation in the ionosphere, Master's Thesis, Hacettepe University, Türkiye.

Koroglu, O. (2012). Statistical analysis of total electron content using TPGN and TPGN-Active network, Master's Thesis, Hacettepe University, Türkiye.

Koroglu, M. and F. Arikan (2020). Spatio-temporal analysis of ionospheric disturbances for ground based augmentation systems over a midlatitude region, Adv. Space Res., 65, 9, 2099-2118.

Lu, W., G. Ma and Q. Wan (2021). A review of voxel-based computerized ionospheric tomography with GNSS ground receivers, Remote Sensing, 13, 3432, doi:10.3390/rs13173432.

Mitchell, C. N. and P. S. Spencer (2003). A three-dimensional time-dependent algorithm for ionospheric imaging using GPS. Ann. Geophys., 46, 687-696.

Nayir, H., F. Arikan, O. Arikan and C. Erol (2007). Total electron content estimation with Reg-Est, J. Geophys. Res.: Space Phys., 112, doi:10.1029/2007JA012459.

Nielsen, F. and R. Nock (2009). Sided and symmetrized Bregman centroids, IEEE Trans. Info. Theory, 55, 2882-2904, doi:10.1109/TIT.2009.2018176.

Raymund, T. D., J. R. Austen, S. Franke, C. Liu et al. (1990). Application of computerized tomography to the investigation of ionospheric structures, Radio Sci., 25, 771-789, doi:10.1029/RS025i005p00771.

Sayin, I., F. Arikan and O. Arikan (2008). Regional TEC mapping with random field priors and kriging, Radio Sci., 43, 05, 1-14.

Sayin, I., F. Arikan and K. Akdogan (2010). Optimum temporal update periods for regional ionosphere monitoring, Radio Sci., 45, 1-9, doi:10.1029/2009RS004316.

Sezen, U., F. Arikan, O. Arikan, O. Ugurlu and A. Sadeghimorad (2013). Online, automatic, near-real time estimation of GPS-TEC: IONOLAB-TEC, Space Weather, 11, 297-305, doi:10.1002/swe.20054.

Sezen, U., T. L. Gulyaeva and F. Arikan (2018). Performance of solar proxy options of IRI-Plas model for equinox seasons, J. Geophys. Res.: Space Phys., 123, 1441-1456, doi:10.1002/2017JA024994.

Spencer, P. S. and C. N. Mitchell (2007). Imaging of fast moving electron-density structures in the polar cap, Ann. Geophys., 50, 3, 427-434.

Ssessanga, N., Y. H. Kim, J. B Habarulema and Y. S. Kwak (2019). On imaging South African regional ionosphere using 4D-var technique, Space Weather, 17, 11, 1584-1604.

Tuna, H., O. Arikan, F. Arikan, T. L. Gulyaeva and U. Sezen (2014). Online user-friendly slant total electron content computation from IRI-Plas: IRI-Plas-STEC, Space Weather, 12, 64-75, doi:10.1002/2013SW000998.

Tuna, H., O. Arikan and F. Arikan (2015). Regional model-based computerized ionospheric tomography using GPS measurements: IONOLAB-CIT, Radio Sci., 50, 1062-1075, doi:10.1002/2015RS005744.

Tuna, H., O. Arikan and F. Arikan (2018). Model based computerized ionospheric tomography in space and time, Adv. Space Res,, 61, 2057-2073, doi:10.1016/j.asr.2018.01.031.

Yavuz, E., F. Arikan, O. Arikan and C. B. Erol (2005). Algorithms and basis functions in tomographic reconstruction of ionospheric electron density, In Proceedings of the 13th European Signal Processing Conference.

Yenen, S., T. Gulyaeva, F. Arikan and O. Arikan (2015). Association of ionospheric storms and substorms of Global Electron Content with proxy AE index, Adv. Space Res., 56, 1343-1353, doi:10.1016/j.asr.2015.06.025.

Yenen, S. D. (2017). Estimation of total electron content and receiver bias for a GPS network, Master's Thesis, Hacettepe University, Türkiye.

Yenen, S. D. and F. Arikan (2024). IONOLAB-Fusion: Fusion of Radio Occultation into Computerized Ionospheric Tomography, Atmosphere, 15, 6, 675, doi:10.3390/atmos15060675.

Yenen, S. D. (2024). Fusion of Radio Occultation into Computerized Ionospheric Tomography, Doctoral Dissertation, Hacettepe University, Türkiye.

Zeilhofer, C., M. Schmidt, D. Bilitza and C. Shum (2009). Regional 4-D modeling of the ionospheric electron density from satellite data and IRI, Adv. Space Res., 43, 1669-1675, doi:10.1016/j.asr.2008.09.033.

Zhai, C., G. Lu, Y. Yao, W. Wang, et al. (2020). 3-D tomographic reconstruction of SED plume during 17 March 2013 storm, J. Geophys. Res.: Space Phys., 125, e2020JA028257, doi:10.1029/2020JA028257.

***CORRESPONDING AUTHOR: Sinem Deniz YENEN**,
Hacettepe University, Electrical and Electronics Engineering, Ankara, Türkiye
e-mail: sdyenen@aselsan.com